CRASH: A BLOCK-ADAPTIVE-MESH CODE FOR RADIATIVE SHOCK HYDRODYNAMICS – IMPLEMENTATION AND VERIFICATION

B. van der Holst[1], G. Tóth[1], I.V. Sokolov[1], K.G. Powell[1], J.P. Holloway[1], E.S. Myra[1], Q. Stout[1], M.L. Adams[2], J.E. Morel[2], R.P. Drake[1]

ABSTRACT

We describe the CRASH (Center for Radiative Shock Hydrodynamics) code, a block adaptive mesh code for multi-material radiation hydrodynamics. The implementation solves the radiation diffusion model with the gray or multigroup method and uses a flux limited diffusion approximation to recover the free-streaming limit. The electrons and ions are allowed to have different temperatures and we include a flux limited electron heat conduction. The radiation hydrodynamic equations are solved in the Eulerian frame by means of a conservative finite volume discretization in either one, two, or three-dimensional slab geometry or in two-dimensional cylindrical symmetry. An operator split method is used to solve these equations in three substeps: (1) solve the hydrodynamic equations with shock-capturing schemes, (2) a linear advection of the radiation in frequency-logarithm space, and (3) an implicit solve of the stiff radiation diffusion, heat conduction, and energy exchange. We present a suite of verification test problems to demonstrate the accuracy and performance of the algorithms. The CRASH code is an extension of the Block-Adaptive Tree Solarwind Roe Upwind Scheme (BATS-R-US) code with this new radiation transfer and heat conduction library and equation-of-state and multigroup opacity solvers. Both CRASH and BATS-R-US are part of the publicly available Space Weather Modeling Framework (SWMF).

Subject headings: hydrodynamics – methods: numerical – radiative transfer

1. INTRODUCTION

As photons travel through matter, the radiation field experiences changes due to net total emission, absorption, and scattering, see for instance Mihalas & Mihalas (1984); Pomraming (2005); Drake (2006). At high enough energy density the radiation will heat and accelerate the plasma. This coupled system is radiation hydrodynamics. The radiation can at a fundamental level be described by the time evolution of the spectral radiation intensity $I_\nu(\mathbf{r}, t, \mathbf{n}, \nu)$, which is the radiation energy per unit area, per unit solid angle in the direction of photon propagation $\mathbf{n}$, per unit interval of photon frequency ν, and per unit time interval. Several method have been developed to solve the radiation field in various degree of physics fidelity.

In Monte Carlo radiative transfer methods, the radiation is statistically evaluated. Small photon packets are created with their energy and propagation direction statistically selected. The packets are propagated through matter using the radiation transfer equation (Nayakshin et al. 2009; Maselli et al. 2009; Baek et al. 2009). Characteristic methods use integration along rays of various lengths to solve for the

---

[1]University of Michigan, Ann Arbor, MI 48109, USA

[2]Texas A&M University, College Station, TX, USA

angular structure of the radiation transport. A recent conservative, causal ray-tracing method was developed and combined with a short characteristic ray-tracing for the transfer calculations of ionizing radiation (Mellema et al. 2006). Solar surface magneto-convection simulations are increasingly realistic and use a three-dimensional, non-gray, approximate local thermodynamic equilibrium (LTE), radiative transfer for the heating and cooling of plasma. These simulations are typically formulated for four frequency bins in the radiative transport equation (Vögler et al. 2005; Stein et al. 2007; Martínez-Sykora et al. 2009).

For some applications, simplifications to the radiation transfer can be made by calculating moments of the radiation intensity over the solid angle Ω. The spectral radiation energy and the spectral radiation energy flux are defined by the 0th and 1st moments as

$$E_\nu(\mathbf{r}, t, \nu) = \frac{1}{c} \int_{4\pi} I_\nu(\mathbf{r}, t, \mathbf{n}, \nu) d\Omega, \qquad \mathbf{F}_\nu(\mathbf{r}, t, \nu) = \int_{4\pi} \mathbf{n} I_\nu(\mathbf{r}, t, \mathbf{n}, \nu) d\Omega. \tag{1}$$

In addition, the spectral radiation pressure tensor $\mathbf{P}_\nu$ is defined by the second moment

$$\mathbf{P}_\nu(\mathbf{r}, t, \nu) = \frac{1}{c} \int_{4\pi} \mathbf{nn} I_\nu(\mathbf{r}, t, \mathbf{n}, \nu) d\Omega. \tag{2}$$

A whole class of radiation transfer models are based on solving the corresponding radiation moment equations, using a closure relation between the spectral pressure tensor and the spectral intensity (Mihalas & Mihalas 1984; Pomraming 2005; Drake 2006).

A radiation-hydrodynamics code based on variable Eddington tensor (VET) methods (Stone et al. 1992) can still capture the angular structure of the radiation field by relating the spectral radiation pressure tensor to the spectral radiation intensity and the method is applicable for both the optically thin and thick regime. Optically thin versions of the VET method have been used in the context of cosmological reionization (Petkova & Springel 2009).

Further simplification assumes that the radiation pressure is isotropic and proportional to the radiation energy. This is the diffusion approximation. Several codes have been developed using this approximation. HYDRA (Marinak 2001) is an arbitrary Lagrange Eulerian code for 2D and 3D radiation hydrodynamics. The radiation transfer model is based upon either flux limited multigroup or implicit Monte Carlo radiation transport. The Eulerian code RAGE (Gittings et al. 2008) uses a cell-based adaptive mesh refinement to achieve resolved radiative hydrodynamic flows. HYADES (Larsen & Lane 1994) solve the radiation hydrodynamic equations on a Lagrangian mesh, while CALE (Barton 1985) can use either a fixed Eulerian mesh, an embedded Lagrangian mesh, or a partially embedded, partially remapped mesh. Our newly developed radiation-hydrodynamic solver uses an Eulerian grid together with a block-based adaptive mesh refinement strategy.

We limit the discussion of the radiation hydrodynamics implementation in CRASH to plasmas in the absence of magnetic field. Most of the description in this paper can, however, easily be extended to magnetohydrodynamic (MHD) plasmas as well. Indeed, since the CRASH code is essentially the magnetohydrodynamic BATS-R-US code (Powell et al. 1999; Toth et al. 2010) extended with libraries containing radiation transport, equation-of-state (EOS), and opacity solvers, the implementation for the coupling between the radiation field and MHD plasmas is readily available. The CRASH code uses the recently developed block adaptive tree library (BATL, Toth et al. (2010)). Here we will focus on the radiation implementation. Both the CRASH and BATS-R-US codes are publicly available as part of the Space Weather Modeling Framework (SWMF, Toth et al. (2005)) or can be used as stand-alone codes.

In the following, Section 2 introduces the radiation hydrodynamic equations for multi-material plasmas, in a form general enough to apply at high energy density. Section 3 describes the numerical algorithms

to solve these equations. Next, in Section 4 verification tests, are presented for radiation and electron heat conduction on non-uniform meshes in 1D, 2D, and 3D slab geometry and in axially symmetric (rz) geometry. We also show a full system multi-material radiation hydrodynamic simulation on an adaptively refined mesh and demonstrate good scaling up to 1000 processors. The paper is summarized in Section 5.

2. EQUATIONS OF RADIATION HYDRODYNAMICS IN DENSE PLASMAS

The equations of radiation hydrodynamics describe the time evolution of both matter and radiation. For the applications that supported the work reported here, the code must be able to model matter as a high energy density plasma that is in LTE so that the population of all atomic and ion states can be obtained from statistical physics (see for instance Landau & Lifshitz (1980)). We allow for multiple materials throughout the spatial domain of interest, but restrict the analysis to plasma flows that are far from relativistic. The materials can be heated to sufficiently high temperatures so that they can ionize and create free electrons, introducing the need for a time evolution equation for the electron energy density. The electrons transfer heat by thermal heat conduction and emit and absorb photon radiation. The radiation model discussed in this paper is non-equilibrium diffusion, in which the electron and radiation temperature can be different. We approximate the radiation transfer with a gray or multigroup flux limited diffusion (FLD). This model is also of interest for application to a number of astrophysical problems.

In the following subsections, we will describe the radiative transfer equations for the evolution of the multigroup radiation energy densities (Section 2.1) in the FLD approximation (Section 2.5). The coupling of the radiation field to the two species hydrodynamic equations of electrons and ions are discussed in Section 2.2. In Section 2.3, the method for tracking the different materials is treated, while the lookup tables used for of the EOS and opacities are mentioned in Section 2.4.

2.1. Radiation Transport

In this section, we will build up the form of the radiation transport in the multigroup diffusion approximation that is used for the implementation in the CRASH code. The spectral pressure tensor, equation (2), is often approximated in the form (Mihalas & Mihalas 1984)

$$\mathbf{P}_\nu(\mathbf{r}, t, \nu) = E_\nu \mathbf{T}_\nu, \tag{3}$$

where

$$\mathbf{T}_\nu(\mathbf{r}, t, \nu) = \frac{1}{2}(1 - \chi_\nu)\mathbf{I} + \frac{1}{2}(3\chi_\nu - 1)\frac{\mathbf{F}_\nu \mathbf{F}_\nu}{|\mathbf{F}_\nu|^2}, \tag{4}$$

is the spectral Eddington tensor, χ_ν is the Eddington factor, and $\mathbf{I}$ is the identity matrix. The second term on the right hand side is a dyad constructed from the direction of the spectral radiation flux. The pressure tensor can be used to arrive at a time evolution equation for the solid angle integrated spectral radiation energy (Buchler 1983)

$$\frac{\partial E_\nu}{\partial t} + \nabla \cdot (E_\nu \mathbf{u}) - \nu \frac{\partial}{\partial \nu}(\mathbf{P}_\nu : \nabla \mathbf{u}) = \text{diffusion} + \text{emission} - \text{absorption}, \tag{5}$$

which contains the plasma velocity $\mathbf{u}$ of the background plasma. Here the colon denotes the contraction of the two tensors $\mathbf{P}_\nu$ and $\nabla \mathbf{u}$. The processes described by the symbolic terms on the right hand side of equation (5) will be described below.

Setting the Eddington factor $\chi_\nu = 1/3$ corresponds to the radiation diffusion model. In this case the radiation is assumed to be effectively isotropic and the spectral radiation pressure can be described by the scalar

$$p_\nu = \frac{1}{3}E_\nu = (\gamma_r - 1)E_\nu, \tag{6}$$

where we have introduced the adiabatic index of the radiation field, which in this case has the relativistic value $\gamma_r = 4/3$. The time evolution for the spectral energy density can then be simplified to

$$\frac{\partial E_\nu}{\partial t} + \nabla \cdot (E_\nu \mathbf{u}) - (\gamma_r - 1)(\nabla \cdot \mathbf{u})\nu\frac{\partial E_\nu}{\partial \nu} = \text{diffusion} + \text{emission} - \text{absorption}. \tag{7}$$

The second and third terms on the left hand side of equation (7) express the change in the spectral energy density due to the advection and compression of the background plasma, which moves with the velocity $\mathbf{u}$, as well as the frequency shift due to compression. In the free-streaming limit where the radiation hardly interacts with the matter, χ_ν will approach one. In this paper we will keep $\chi_\nu = 1/3$ and at the same time use a flux limited diffusion for the free-streaming regime whenever needed (see Section 2.5).

The set of equations for the spectral energy density (7) still consists of an infinite amount of equations, one for each frequency. A finite set of governing equations to describe the radiation transport in the multi-group diffusion approximation is obtained when we choose a set of frequency groups. Here we enumerate groups with the index, $g = 1, \ldots, G$. The interval of the photon frequencies, relating to the gth group is denoted as $[\nu_{g-1/2}, \nu_{g+1/2}]$. A discrete set of group energy densities, E_g, is introduced in terms of the integrals of the spectral energy density of the frequency group interval:

$$E_g = \int_{\nu_{g-1/2}}^{\nu_{g+1/2}} E_\nu d\nu. \tag{8}$$

Now we can integrate equation (7) to arrive at the desired set of the multigroup equations:

$$\begin{aligned}
\frac{\partial E_g}{\partial t} &+ \nabla \cdot (E_g\mathbf{u}) + (\gamma_r - 1)E_g\nabla \cdot \mathbf{u} - (\gamma_r - 1)(\nabla \cdot \mathbf{u})\int_{\nu_{g-1/2}}^{\nu_{g+1/2}} \frac{\partial(\nu E_\nu)}{\partial \nu}d\nu \\
&= \int_{\nu_{g-1/2}}^{\nu_{g+1/2}} (\text{diffusion} + \text{emission} - \text{absorption})d\nu.
\end{aligned} \tag{9}$$

The fourth term on the left hand side is a frequency shift due to the plasma compression. This term is essentially a conservative advection along the frequency axis.

In the context of the multi-group radiation diffusion, a discussion about the stimulated emission is not less important than LTE. Excellent accounts on the stimulated emission exist in the literature, see for instance Zel'dovich & Raizer (2002). Here, we merely sumarize how the stimulated emission modifies the absorption opacity κ_ν^a obtained from, e.g., opacity tables. This is important when dealing with externally supplied opacity tables, since the CRASH code assumes that the absorption opacities are corrected. Integrating the total absorption and emission over all directions and summing up the two polarizations of the photons, the following expression can be derived for the emission and absorption

$$\text{emission} - \text{absorption} = c\kappa_\nu^{a'}\left(B_\nu - E_\nu\right), \tag{10}$$

where the effective absorption coefficient, $\kappa_\nu^{a'}$, is introduced to account for the correction due to stimulated emission:

$$\kappa_\nu^{a'} = \kappa_\nu^a\left(1 - \exp\left[-\frac{\varepsilon}{k_B T_e}\right]\right), \tag{11}$$

in which $\varepsilon = h\nu$ is the photon energy, k_B is the Boltzmann constant, and T_e is the electron temperature. We also introduced the spectral energy density distribution of the black body radiation (the Planckian)

$$B_\nu = \frac{8\pi}{h^3 c^3} \frac{\varepsilon^3}{\exp[\varepsilon/(k_B T_e)] - 1}. \tag{12}$$

The total energy density in the Planck spectrum equals $B = \int_0^\infty d\nu B_\nu = aT_e^4$, where $a = 8\pi^5 k_B^4/(15h^3 c^3)$ is the radiation constant.

We use the standard definition of the group Planck mean opacity κ_{Pg} and group Rosseland mean opacity κ_{Rg} (Mihalas & Mihalas 1984)

$$\kappa_{Pg} = \frac{\int_{\nu_{g-1/2}}^{\nu_{g+1/2}} d\nu \kappa_\nu^{a\prime} B_\nu}{B_g}, \qquad \kappa_{Rg} = \frac{\frac{\partial B_g}{\partial T_e}}{\int_{\nu_{g-1/2}}^{\nu_{g+1/2}} d\nu \frac{1}{\kappa_\nu^t} \frac{\partial B_\nu}{\partial T_e}}, \qquad B_g = \int_{\nu_{g-1/2}}^{\nu_{g+1/2}} d\nu B_\nu \tag{13}$$

in which κ_ν^t is the spectral total opacity. The right hand side of equation (9) can now be written as (see for instance Mihalas & Mihalas (1984); Pomraming (2005))

$$\frac{\partial E_g}{\partial t} + \nabla \cdot (E_g \mathbf{u}) + (\gamma_r - 1)E_g \nabla \cdot \mathbf{u} - (\gamma_r - 1)\nabla \cdot \mathbf{u} \int_{\nu_{g-1/2}}^{\nu_{g+1/2}} \frac{\partial(\nu E_\nu)}{\partial \nu} d\nu$$
$$= \nabla \cdot (D_g \nabla E_g) + \sigma_g (B_g - E_g), \tag{14}$$

where $D_g = c/(3\kappa_{Rg})$ is the radiation diffusion coefficient for radiation group g. The absorption and emission uses the coefficient $\sigma_g = c\kappa_{Pg}$. These group mean opacities are either supplied by lookup tables or by an opacity solver.

In a single group approximation (gray diffusion), the spectral energy density is integrated over all photon frequencies and the total radiation energy density is obtained by

$$E_r(\mathbf{r}, t) = \int_0^\infty E_\nu d\nu. \tag{15}$$

This amounts to summing up all groups $E_r = \sum_g E_g$. The gray radiation diffusion equation can be derived as (see for instance Mihalas & Mihalas (1984); Pomraming (2005); Drake (2006))

$$\frac{\partial E_r}{\partial t} + \nabla \cdot (E_r \mathbf{u}) + (\gamma_r - 1)E_r \nabla \cdot \mathbf{u} = \nabla \cdot (D_r \nabla E_r) + \sigma_r (B - E_r), \tag{16}$$

where the diffusion coefficient D_r is now defined by the single group Rosseland mean opacity κ_R as $D_r = c/(3\kappa_R)$, and the absorption coefficent σ_r is defined in terms of the single group Planck mean opacity κ_P as $\sigma_r = c\kappa_P$.

2.2. Hydrodynamics

In the CRASH code, a single fluid description is used, so that all of the atomic and ionic species as well as the electrons move with the same bulk velocity $\mathbf{u}$. The conservation of mass

$$\frac{\partial \rho}{\partial t} + \nabla \cdot (\rho \mathbf{u}) = 0, \tag{17}$$

provides the time evolution of the mass density ρ of all the materials in the simulation. The plasma velocity is obtained from the conservation of momentum

$$\frac{\partial \rho \mathbf{u}}{\partial t} + \nabla \cdot [\rho \mathbf{uu} + I(p + p_r)] = 0. \tag{18}$$

The total plasma pressure is the sum of the ion and electron pressures: $p = p_i + p_e$. The net force of the radiation on the plasma is given by the gradient of the total radiation pressure $-\nabla p_r$, where the total radiation pressure is obtained from the group radiation energies: $p_r = (\gamma_r - 1) \sum E_g$.

In a high density plasma, the electrons are very strongly coupled to the ions by collisions. However, for higher temperatures, the electrons and ions get increasingly decoupled. At a shock front, where ions are preferentially heated by the shock wave, the electrons and ions are no longer in temperature equilibrium. Ion energy is transfered to the electrons by collisions, while the electrons will in turn radiate energy. We therefore solve separate equations for the ion/atomic internal energy density E_i and the electron internal energy density E_e:

$$\frac{\partial E_i}{\partial t} \quad + \quad \nabla \cdot (E_i \mathbf{u}) + p_i \nabla \cdot \mathbf{u} = \sigma_{ie}(T_e - T_i), \tag{19}$$

$$\frac{\partial E_e}{\partial t} \quad + \quad \nabla \cdot (E_e \mathbf{u}) + p_e \nabla \cdot \mathbf{u} = \nabla \cdot (C_e \nabla T_e) + \sigma_{ie}(T_i - T_e) + \sum_{g=1}^{G} \sigma_g (E_g - B_g). \tag{20}$$

The coupling coefficient $\sigma_{ie} = n_a k_B / \tau_{ie}$ in the collisional energy exchange between the electrons and ions depends on the relaxation time $\tau_{ie}(T_e, n_a, m)$ and the atomic number density n_a. The energy transfer depends also on the difference between the ion temperature T_i and the electron temperature T_e. In equation (20), we have included the electron thermal heat conduction with conductivity $C_e(T_e, n_a, m)$. Since the electrons are the species that are responsible for the radiation absorption and emission, the energy exchange between the electrons and the radiation groups is added to equation (20).

For the development of the numerical schemes in Section 3 we will use an equation for the conservation of the total energy density

$$e = \frac{\rho u^2}{2} + E_i + E_e + \sum_{g=1}^{G} E_g, \tag{21}$$

instead of the equation for the ion internal energy (19). This is especially important in regions of the computational domain where hydrodynamic shocks can occur, so that we can recover the correct jump conditions. The conservation of the total energy can be derived from equations (14) and (17)–(20) as

$$\frac{\partial e}{\partial t} + \nabla \cdot [(e + p + p_r)\mathbf{u}] = \nabla \cdot (C_e \nabla T_e) + \sum_{g=1}^{G} \nabla \cdot (D_g \nabla E_g). \tag{22}$$

The frequency shift term in equation (14) due to the plasma compression does not show up in the conservation of the total energy if we use energy conserving boundary conditions at the end points of the frequency domain, i.e. at $\nu = 0$ and $\nu = \infty$ in the analytical description or at the end points of the numerically truncated finite domain.

2.3. Level Sets and Material Identification

In many of the CRASH applications, we need a procedure to distinguish between different materials. We assume that the materials do not mix, but differ from each other by their properties such as the equation

of state and opacities. If we use M different materials, then we can define for each material $m = 1, \ldots, M$ the level set function $d_m(\mathbf{r}, t)$ that is initially set to zero at the material interface, while positive inside the material region and negative outside. Generally, we use a smooth and signed distance function in the intial state. At later times, the location of material m is obtained by means of a simple advection equation

$$\frac{\partial d_m}{\partial t} + \nabla \cdot (d_m \mathbf{u}) = d_m \nabla \cdot \mathbf{u}. \tag{23}$$

For any given point in space and time, we can determine what the material is, since analytically only one of the level set functions d_m can be positive at any given point. Numerical errors will create regions where this is not true. In practice we take the largest d_m. This is a simple approximation, we may explore more sophisticated approaches in the future. The number of material levels M can be configured at compile time.

2.4. Equation of State and Opacities

We have implemented EOS solvers and a code to calculate the frequency averaged group opacities. The implemention will be reported elsewhere, but mention that in the EOS and opacity solver the temperature is assumed to be well below the relativistic values: $T \ll 10^5$ eV. The non-relativistic speed of motion is also assumed while simplifying the radiation transport equation and to neglect the relativistic corrections for opacities. In this paper, we will assume that all necessary quantities are calculated and stored in lookup tables. Our EOS solver assumes that the corrections associated with ionization, excitation, and Coulomb interactions of the partially ionized ion-electron plasma are all added to the energy of the electron gas and to the electron pressure. This is possible since those corrections are controlled by the electron temperature. The ion internal energy density, ion pressure, and ion specific heat in an isochoric process per unit of volume are simply

$$p_i = n_a k_B T_i, \qquad E_i = \frac{p_i}{\gamma - 1}, \qquad C_{Vi} = \left(\frac{\partial E_i}{\partial T_i} \right)_\rho = \frac{n_a k_B}{\gamma - 1}, \tag{24}$$

which are due to the contributions due to ion translational motions for which $\gamma = 5/3$.

The relations among the electron internal energy density, pressure, density, and temperature are known as the EOS. To solve these relations is usually complex and time consuming. We therefore store these relations in invertible lookup tables. For each material m, our EOS tables have the logarithmic lookup arguments $(\log T_e, \log n_a)$. The list of quantities stored in these tables is indicated in Table 1. These lookup tables are populated with quantities that are needed for both single temperature and two temperature simulations. For two-temperature plasma simulations, we will need p_e, E_e, the electron specific heat C_{Ve}, the electron speed of sound gamma γ_{S_e}. For convenience we added the total pressure $p = p_e + p_i$, total internal energy density $E = E_i + E_e$, single temperature specific heat C_V, and the single temperature speed of sound gamma γ_S, which can be used in single temperature simulations. We use high enough table resolutions so that it is sufficient to use a bilinear interpolation in the lookup arguments. If p_e or E_e (or p and E in single temperature mode) are known on entry of the lookup instead of T_e, we do a binary search in the table to find the appropriate electron temperature. The latter only works as long as the necessary thermodynamic derivatives are sign definite, i.e. the table is invertible. Other thermodynamic quantities that are needed, but not stored in these lookup tables, can be derived. For example, the electron density can be obtained from the mean ionization $n_e = n_a \overline{Z}$.

In addition, we have lookup tables for the averaged multigroup opacities. These tables are either constructed internally for a given frequency range, number of groups, and the selected materials, or externally

supplied. For any material m, the logarithmic lookup arguments are $(\log \rho, \log T_e)$. The stored quantities, see Table 2, are the specific Rosseland mean opacity κ_{Rg}/ρ and the specific Planck mean opacity κ_{Pg}/ρ for all groups $g = 1, \ldots, G$ that are used during a simulation. The Planck opacities are assumed to be corrected for the stimulated emission, as discussed in Section 2.1. The groups are always assumed to be logarithmically distributed in the frequency space.

2.5. Flux Limited Diffusion

Radiation diffusion theory can transport energy too fast in the optically thin free streaming limit. In the diffusion limit, the radiation diffusion flux for each group follows Fick's law $\mathbf{F}_g = -D_g \nabla E_g$, where the diffusion coefficient D_g depends on the Rosseland mean opacity κ_{Rg} for the group g via $D_g = c/(3\kappa_{Rg})$. This flux is however not bounded. In the optically thin free-streaming limit, the magnitude of the radiation flux can be at most cE_g in order to maintain causality. Various flux limiters exist in the literature, see for instance Minerbo (1978); Lund & Wilson (1980); Levermore & Pomraming (1981), that ensure that the diffusion flux is limited by this free streaming flux. We implemented the so-called square-root flux limiter to obtain the correct progation speed in the optically thin regime (Morel 2000). For this flux limiter, the diffusion coefficient is rewritten as

$$D_g = \frac{c}{\sqrt{(3\kappa_{Rg})^2 + \frac{|\nabla E_g|^2}{E_g^2}}}. \tag{25}$$

In the limit that the radiation length scale $L_R = E_g/|\nabla E_g|$ is large, the diffusive limit is recovered. For a small radiation length scale, $D_g = c|E_g|/|\nabla E_g|$ and the radiation propagates with the speed of light.

Similarly, we implemented the option to limit the electron thermal heat flux (see Drake (2006) for more details on electron flux limiters). The classical Spitzer-Harm formula for the collisional electron conductivity is proportional to $T_e^{5/2}/\overline{Z^2}$, where $\overline{Z^2}$ is the mean square ionization of the used material. The collisional model is only valid when the temperature scale length $L_T = T_e/|\nabla T_e|$ is much larger than the collisional mean free path of the electrons λ_{mfp}. When the temperature scale length is only a few λ_{mfp} or smaller, this description breaks down. This may for instance happen in laser-irradiated plasmas. One could in that case find the heat flux from solving the Fokker-Planck equation for the electrons, but this is computationally expensive. Instead, we use a simplified model to limit the electron heat flux. A free-streaming heat flux can be defined as the thermal energy density in the plasma transported at some characteristic thermal velocity: $F_{FS} = n_e k_B T_e v_{th}$, where $v_{th} = \sqrt{k_B T_e/m_e}$. For practical applications, the maximum heat transport is usually only a fraction of this free-streaming flux: $\mathbf{F} = -(f F_{FS}/|\nabla T_e|)\nabla Te$, where f is the so-called flux limiter. This heat flux model is the threshold model and is also used in other radhydro packages, such as HYADES (Larsen & Lane 1994). The flux-limited heat flux can now be defined as

$$\mathbf{F} = -\min\left(C_e, \frac{f F_{FS}}{|\nabla T_e|}\right)\nabla T_e. \tag{26}$$

The flux limiter f is an input parameter and can be tuned to let the simulated results better fit reality.

3. THE NUMERICAL METHOD

In this section, we describe the discretization of the set of multi-material, radiation hydrodynamics equations for the density (17), momentum (18), total energy (22), electron internal energies (20), radiation

group energy (14), and material level set functions (23). The equations are time integrated using an operator split method to solve the equations in substeps. Formally, we may write this system as

$$\frac{\partial \mathbf{U}}{\partial t} = \mathbf{R}_{\text{hydro}}(\mathbf{U}) + \mathbf{R}_{\text{frequency}}(\mathbf{U}) + \mathbf{R}_{\text{diffusion}}(\mathbf{U}), \tag{27}$$

where $\mathbf{U}$ is the vector of state variables. We have split the right hand sides of the equations into three parts and time advance the equations with an operator splitting method in the following order: (1) The right hand side $\mathbf{R}_{\text{hydro}}$ describes the advection and pressure contributions (Section 3.1). This part is essentially the ideal hydrodynamic equations augmented with the advection and compression of the radiation energy, the electron internal energy, and the material level sets. (2) The right hand side $\mathbf{R}_{\text{frequency}}$ is the advection of the radiation field in frequency space (Section 3.2). (3) The right hand side $\mathbf{R}_{\text{diffusion}}$ takes care of the diffusion and energy exchange terms, which we will solve with an implicit scheme (Section 3.3). The operator splitting is not unique. Instead of splitting the hydrodynamic advection operator and the extra advance operator for the frequency advection, one may attempt to discretize the frequency advection flux as an extra flux for the control volume of the four-dimensional (x, y, z, ν) space. However, since the CRASH code is built around the existing BATS-R-US code in 1D, 2D, and 3D, we opted for splitting the frequency advection from the hydro update. The boundary conditions are treated in Section 3.4.

3.1. Hydro Solve

In the first step of the operator splitting, we update the hydrodynamic equations including the advection and compression of the radiation energy density, electron internal energy density and the level sets. We have implemented two variants to solve the hydrodynamic equations: (1) using conservation of the total energy (Section 3.1.1) and (2) a non-conservative pressure formulation (Section 3.1.2). We can combine the two discretizations in a hybrid manner a simulation.

3.1.1. Conservative

We have implemented several hydrodynamic shock-capturing schemes in the CRASH code: the HLLE scheme (Harten et al. 1983; Einfeldt et al. 1991), the Rusanov scheme (Yee 1989), and a Godunov scheme (Godunov 1959) with an exact Riemann solver. In this section, we will explain how we generalized the HLLE scheme for our system of equations that includes radiation, level sets, and an EOS. The other hydrodynamic schemes can be generalized in a similar fashion.

Typical hydrodynamic solvers in the literature assume constant γ. Our problem is to generalize the constant γ hydro solvers for the case of spatially varying polytropic index, γ_e, due to ionization, excitation and Coulomb interactions. A method that is applicable to all the aforementioned, constant γ, hydrodynamic shock-capturing schemes is to split the electron internal energy E_e density as the sum of an ideal (translational) energy part $p_e/(\gamma - 1)$ and an extra internal energy density E_X. Similarly, we can define an ideal total energy density

$$e_I = \frac{\rho u^2}{2} + \frac{p_i + p_e}{\gamma - 1} + \sum_{g=1}^{G} E_g, \tag{28}$$

which is related to the total energy density by $e = e_I + E_X$. We will time advance p_e with the ideal electron pressure equation and E_X by a conservative advection equation, and then apply a correction step as described below.

The time update with the operator $\mathbf{R}_{\text{hydro}}$ solves the following equations:

$$\frac{\partial \rho}{\partial t} \quad + \quad \nabla \cdot (\rho \mathbf{u}) = 0, \tag{29}$$

$$\frac{\partial \rho \mathbf{u}}{\partial t} \quad + \quad \nabla \cdot [\rho \mathbf{u}\mathbf{u} + I(p + p_r)] = 0, \tag{30}$$

$$\frac{\partial e_I}{\partial t} \quad + \quad \nabla \cdot [(e_I + p + p_r)\mathbf{u}] = 0, \tag{31}$$

$$\frac{1}{\gamma - 1}\frac{\partial p_e}{\partial t} \quad + \quad \frac{1}{\gamma - 1}\nabla \cdot (p_e \mathbf{u}) + p_e \nabla \cdot \mathbf{u} = 0, \tag{32}$$

$$\frac{\partial E_X}{\partial t} \quad + \quad \nabla \cdot [E_X \mathbf{u}] = 0, \tag{33}$$

$$\frac{\partial E_g}{\partial t} \quad + \quad \nabla \cdot (E_g \mathbf{u}) + (\gamma_r - 1)E_g \nabla \cdot \mathbf{u} = 0, \tag{34}$$

$$\frac{\partial d_m}{\partial t} \quad + \quad \nabla \cdot (d_m \mathbf{u}) - d_m \nabla \cdot \mathbf{u} = 0, \tag{35}$$

where the frequency advection, diffusion, and energy exchange terms are ommitted in this first operator step. After each time advance from time t^n to time t^{n+1}, we have to correct e, e_I, p_e, and E_X. We denote the uncorrected variables with a superscript $*$, then we recover at time level $n + 1$ the true electron internal energy E_e^{n+1} and the true total energy density e^{n+1} by

$$E_e^{n+1} \quad = \quad \frac{p_e^*}{\gamma - 1} + E_X^*, \tag{36}$$

$$e^{n+1} \quad = \quad e_I^* + E_X^*. \tag{37}$$

Since both e_I and E_X follow a conservation law, the total energy density e is also conserved. The true electron pressure is recovered from the updated electron internal energy and mass density by means of the EOS:

$$p_e^{n+1} = p_{\text{EOS}}(\rho^{n+1}, E_e^{n+1}, m), \tag{38}$$

where the function p_{EOS} can be either a calculated EOS or an EOS lookup table for material m, determined by the level set functions d_m^{n+1} (Section 2.3). The extra internal energy E_X is reset as the difference between the true electron internal energy and the ideal electron internal energy for $\gamma = 5/3$:

$$E_X^{n+1} = E_e^{n+1} - \frac{p_e^{n+1}}{\gamma - 1}. \tag{39}$$

This is postive because the EOS state p_{EOS} satisfies $E_e - p_e/(\gamma - 1) \geq 0$ at all times. The ideal part of the total energy density at time level $n + 1$ can now be updated as

$$e_I^{n+1} = e^{n+1} - E_X^{n+1}. \tag{40}$$

We have now recovered e^{n+1}, e_I^{n+1}, p_e^{n+1}, and E_X^{n+1} at time t^{n+1}.

We time advanced the hydrodynamic equations to the time level $*$ with a shock-capturing scheme with a constant $\gamma = 5/3$. For an ideal EOS, the speed of sound of the equations (29)–(34) can be derived as

$$c_s = \sqrt{\frac{\gamma(p_i + p_e) + \gamma_r p_r}{\rho}}, \tag{41}$$

which includes the modifications due to the presence of the total radiation pressure. This speed of sound will be used in the hydro scheme below. Since the CRASH EOS solver always satisfies $E_X \geq 0$ and $\gamma_e \leq 5/3$, the speed of sound for the ideal EOS is always an upper bound for the true speed of sound.

We use shock-capturing schemes to advance the equations (29)–(35). In the following, we denote the (near) conservative variables by $U = (\rho, \rho\mathbf{u}, e_I, p_e, E_X, E_g, d_m)$ and let U be grid cell averages in the standard finite volume sense. If we assume for the moment a 1D grid with spacing Δx, cell center index i and cell face between cell i and $i+1$ identified by half indices $i+1/2$, then we can write the two-stage Runge-Kutta hydro update as

$$U_i^{n+1/2} = U_i^n - \frac{\Delta t}{2\Delta x}\left(f_{i+1/2}^n - f_{i-1/2}^n\right), \tag{42}$$

$$U_i^{n+1} = U_i^n - \frac{\Delta t}{\Delta x}\left(f_{i+1/2}^{n+1/2} - f_{i-1/2}^{n+1/2}\right). \tag{43}$$

where f is the numerical flux. In particular, the HLLE flux f equals the physical flux $F(U_{i+1/2}^R)$ when $c_s^+ = u_i + c_s \leq 0$, $F(U_{i+1/2}^L)$ when $c_s^- = u_i - c_s \geq 0$, and in all other cases it uses the weighted flux

$$f_{i+1/2} = \frac{c_s^+ F(U_{i+1/2}^L) - c_s^- F(U_{i+1/2}^R) + c_s^+ c_s^- (U_{i+1/2}^R - U_{i+1/2}^L)}{c_s^+ - c_s^-}. \tag{44}$$

Here, the left and right cell face states are

$$U_{i+1/2}^L = U_i + \frac{1}{2}\bar{\Delta}^L U_i, \tag{45}$$

$$U_{i+1/2}^R = U_{i+1} - \frac{1}{2}\bar{\Delta}^R U_{i+1}. \tag{46}$$

We use the generalized Koren limiter, and define the limited slopes as

$$\bar{\Delta}^L U_i = \mathrm{minmod}\left[\beta(U_{i+1} - U_i), \beta(U_i - U_{i-1}), \frac{2U_{i+1} - U_i - U_{i-1}}{3}\right], \tag{47}$$

$$\bar{\Delta}^R U_i = \mathrm{minmod}\left[\beta(U_{i+1} - U_i), \beta(U_i - U_{i-1}), \frac{U_{i+1} - U_i - 2U_{i-1}}{3}\right], \tag{48}$$

for the extrapolations from the left and right. This reconstruction can be third order in smooth regions away from extrema (Koren 1993; Toth et al. 2008). The parameter β can be changed between 1 and 2, but in simulations with adaptive mesh refinement we have best experience with $\beta = 3/2$. We generally apply the slope limiters on the primitive variables $(\rho, \mathbf{u}, p_i, p_e, E_X/\rho, E_g, d_m)$, instead of the conservative variables. We apply the slope limiter on E_X/ρ instead of E_X since E_X/ρ is smoother at shocks and across material interfaces. A multi-dimensional update is obtained by adding the fluxes for each direction in a dimensionally unsplit manner.

After each stage of the two step Runge-Kutta, we correct for the EOS effects via the update procedure outlined in equations (36)–(40).

3.1.2. Non-Conservative Pressure Equations

In regions away from shocks it is sometimes more important to preserve pressure balance than to have a shock capturing scheme that recovers the correct jump conditions. This is especially important at material

interfaces. We therefore have implemented the option to solve the hydro part of the pressure equations

$$\frac{\partial p_i}{\partial t} \quad + \quad \nabla \cdot (p_i \mathbf{u}) + (\gamma - 1) p_i \nabla \cdot \mathbf{u} = 0, \tag{49}$$

$$\frac{\partial p_e}{\partial t} \quad + \quad \nabla \cdot (p_e \mathbf{u}) + (\gamma_{Se} - 1) p_e \nabla \cdot \mathbf{u} = 0, \tag{50}$$

instead of the equations for the total energy (31) and the electron internal energy (32). As long as the speed of sound gamma for the electrons

$$\gamma_{S_e} = \frac{\rho}{p_e} \left(\frac{\partial p_e}{\partial \rho} \right)_{S_e} \tag{51}$$

is smaller than $\gamma = 5/3$, the numerical scheme is stable. Contrary to the energy conserving scheme, the pressure based scheme can directly include the EOS and we no longer need the time evolution of the extra internal energy density (33). The EOS contribution in the electron pressure equation (50) is implemented as a source term $-(\gamma_{Se} - \gamma) p_e \nabla \cdot \mathbf{u}$ added to the ideal electron pressure equation.

To facilitate using both the shock capturing properties and the pressure balance at the material interfaces during CRASH simulations, we have several criteria to automatically switch between them accordingly. One of the criteria, for instance, uses a detection of steep pressure gradients as a shock identification. The user can select the magnitude of the pressure gradient above which the scheme switches to the conservative energy equations.

3.2. Frequency Advection

The set of multigroup equations (14) contain an integral over the group photon frequencies. Performing this integration, the frequency advection update by the $\mathbf{R}_{\text{frequency}}$ operator can be written as

$$\frac{\partial E_g}{\partial t} - (\gamma_r - 1)(\nabla \cdot \mathbf{u}) \left[\nu_{g+1/2} E_\nu(\nu_{g+1/2}) - \nu_{g-1/2} E_\nu(\nu_{g-1/2}) \right] = 0. \tag{52}$$

These equations, however, do still depend on the unknown photon frequency ν and the spectral radiation energy density E_ν. We will now restrict the analysis to a frequency grid that is uniformly spaced in the frequency logarithm, i.e.,

$$\ln(\nu_{g+1/2}) - \ln(\nu_{g-1/2}) = \Delta(\ln \nu) = \text{constant}. \tag{53}$$

For large enough number of frequency groups G, the group energy E_g can then be approximated as the product of the photon frequency, spectral radiation energy E_ν, and the logarithmic group spacing $\Delta(\ln \nu)$:

$$E_g = \int_{\nu_{g-1/2}}^{\nu_{g+1/2}} E_\nu d\nu = \int_{\ln \nu_{g-1/2}}^{\ln \nu_{g+1/2}} E_\nu \nu d(\ln \nu) \approx E_\nu \nu \Delta(\ln \nu). \tag{54}$$

Using this approximation in equation (52), we obtain our final form of the frequency advection

$$\frac{\partial E_g}{\partial t} + u_\nu \frac{E_{g+1/2} - E_{g-1/2}}{\Delta(\ln \nu)} = 0, \tag{55}$$

where $u_\nu = -(\gamma_r - 1)\nabla \cdot \mathbf{u}$ is the frequency advection speed. The values $E_{g\pm1/2}$ are to be interpolated from the mesh-centered values E_g towards the group boundaries.

The frequency advection is a conservative linear advection in the log-frequency coordinate, for which the physical flux is defined as $F_{g-1/2} = u_\nu E_{g-1/2}$. For the boundary conditions in the frequency domain we

assume zero radiation flux so that no radiation will leak at the edges of the frequency domain. Equation (55) can be discretized with the one-stage second order upwind scheme

$$E_g^{n+1} = E_g^* - \Delta t \frac{f_{g+1/2} - f_{g-1/2}}{\Delta(\ln \nu)}, \tag{56}$$

where time level $*$ is now the state after the hydro update and the numerical flux is

$$
\begin{aligned}
f_{g-1/2} &= u_\nu \left[E_g - \frac{1 - C}{2} \bar{\Delta}(E_{g+1} - E_g, E_g - E_{g-1}) \right], & u_\nu \leq 0, \\
f_{g-1/2} &= u_\nu \left[E_{g-1} + \frac{1 - C}{2} \bar{\Delta}(E_g - E_{g-1}, E_{g-1} - E_{g-2}) \right], & u_\nu \geq 0.
\end{aligned}
\tag{57}
$$

and we use the superbee limiter (Roe 1986) for the limited slope $\bar{\Delta}$. The Courant-Friedrichs-Levi number $C = |u_\nu| \Delta t / \Delta(\ln \nu)$ depends on the hydrodynamic time-step Δt. If C is larger than one, the frequency advection is sub-cycled with the number of steps equal to the smallest integer value larger than C.

3.3. Implicit Diffusion and Energy Exchange

The stiff parts of the radhyro equations are solved implicitly in an operator split fashion. These stiff parts are the radiation energy diffusion, electron heat conduction, and the energy exchange between the electrons and each energy group g and between the electrons and ions. In this section, we will describe two implicit schemes that are implemented: (1) solving for all radiation groups, electron and ion temperatures in a coupled manner (Section 3.3.1), and (2) solving each radiation group energy and the electron temperature independently (Section 3.3.2). Our strategy for resolution changes is described in Appendix A, while the modifications for the rz-geometry are explained in Appendix B.

3.3.1. Coupled Implicit Scheme

Discretizing the diffusion and energy exchange terms of equations (19)–(20), and (14) implicitly in time leads to

$$\frac{E_i^{n+1} - E_i^*}{\Delta t} = \sigma_{ie}^*(T_e^{n+1} - T_i^{n+1}), \tag{58}$$

$$\frac{E_e^{n+1} - E_e^*}{\Delta t} = \sigma_{ie}^*(T_i^{n+1} - T_e^{n+1}) + \nabla \cdot C_e^* \nabla T_e^{n+1} + \sum_{g=1}^{G} \sigma_g^*(E_g^{n+1} - B_g^{n+1}), \tag{59}$$

$$\frac{E_g^{n+1} - E_g^*}{\Delta t} = \sigma_g^*(B_g^{n+1} - E_g^{n+1}) + \nabla \cdot D_g^* \nabla E_g^{n+1}, \tag{60}$$

where time level $*$ now corresponds to the state after the hydro update and the frequency advection. The coupling coefficients σ_{ie}^* and σ_g^* and the diffusion coefficients C_e^* and D_g^* are taken at time level $*$ (frozen coefficients). One can either (1) solve the coupled system of $G + 2$ equations (58)–(60) implicitly or (2) solve equation (58) for the ion internal energy E_i^{n+1}, substitute the solution back into equation (59), and solve the resulting reduced set of $G + 1$ equations (59)–(60) implicitly. Here we describe the second scheme, because it is more efficient, especially for small number of groups, e.g., for gray radiation diffusion. Note that if we did include ion heat conduction in (60), then we would have to solve the entire coupled system of equations.

First we introduce the ion Planck function $B_i = aT_i^4$ as a new variable similar to the electron Planck function $B = aT_e^4$, and replace E_i and E_e with these variables using the chain rule

$$\frac{\partial E_i}{\partial t} = \frac{\partial E_i}{\partial T_i}\frac{\partial T_i}{\partial B_i}\frac{\partial B_i}{\partial t} = \frac{C_{Vi}}{4aT_i^3}\frac{\partial B_i}{\partial t}, \qquad \frac{\partial E_e}{\partial t} = \frac{C_{Ve}}{4aT_e^3}\frac{\partial B}{\partial t}, \tag{61}$$

in which C_{Vi} and C_{Ve} are the specific heats of the ions and electrons, respectively. Now equation (58) can be replaced with

$$B_i^{n+1} = B_i^* + \Delta t \sigma'_{ie}(B^{n+1} - B_i^{n+1}), \tag{62}$$

where

$$\sigma'_{ie} = \sigma_{ie}^* \frac{4aT_i^3}{C_{Vi}}\frac{1}{a(T_e + T_i)(T_e^2 + T_i^2)}, \tag{63}$$

is again taken at time level $*$. The numerator comes from $(T_e^4 - T_i^4)/(T_e - T_i)$. Equation (62) can be solved for B_i^{n+1}. This result can be substituted into the electron internal energy equation (59) to obtain

$$\frac{C'_{Ve}}{\Delta t}(B^{n+1} - B^*) = \sigma''_{ie}(B_i^* - B^{n+1}) + \nabla \cdot C'_e \nabla B^{n+1} + \sum_{g=1}^{G} \sigma_g^*(E_g^{n+1} - w_g^* B^{n+1}), \tag{64}$$

where we have introduced new coefficients at time level $*$:

$$\sigma''_{ie} = \frac{C_{Vi}}{4aT_i^3}\frac{\sigma'_{ie}}{1 + \Delta t \sigma'_{ie}}, \qquad C'_e = \frac{C_e^*}{4aT_e^3}, \qquad C'_{Ve} = \frac{C_{Ve}^*}{4aT_e^3}. \tag{65}$$

The Planck weights $w_g^* = B_g^*/B^*$ satisfy $\sum_g w_g = 1$. It is convenient to introduce the changes $\Delta B = B^{n+1} - B^*$ and $\Delta E_g = E_g^{n+1} - E_g^*$ to arrive at

$$\left[\frac{C'_{Ve}}{\Delta t} + \sigma''_{ie} - \nabla \cdot C'_e \nabla\right]\Delta B \quad - \quad \sum_{g=1}^{G}\sigma_g^*(\Delta E_g - w_g^*\Delta B) = \sigma''_{ie}(B_i^* - B^*)$$

$$+ \quad \nabla \cdot C'_e \nabla B^* + \sum_{g=1}^{G}\sigma_g^*(E_g^* - w_g^* B^*), \tag{66}$$

$$\left[\frac{1}{\Delta t} - \nabla \cdot D_g^* \nabla\right]\Delta E_g \quad - \quad \sigma_g^*(w_g^*\Delta B - \Delta E_g) = \sigma_g^*(w_g^* B^* - E_g^*) + \nabla \cdot D_g^* \nabla E_g^*. \tag{67}$$

This is a coupled system of $G + 1$ linearized equations for the changes ΔB and ΔE_g. The right hand sides are all at time level *.

A discrete set of equations are obtained by applying the standard finite volume method to the equations (66) and (67) and partitioning the domain in a set of control volumes V_i, enumerated by a single index $i = 1, \ldots, I$. As an example, the fluxes F_{gij} associated with the radiation diffusion operator may be obtained by approximating the gradient of the group energy density with a simple central difference in the uniform part of the mesh:

$$-\int_{V_i}\nabla \cdot (D_g \nabla E_g)dV = \sum_j F_{gij} = \sum_j S_{ij}D_{gij}\frac{E_{gi} - E_{gj}}{|\mathbf{x}_i - \mathbf{x}_j|}, \tag{68}$$

where the index j enumerates the control volumes which have a common face with the control volume i, the face area being S_{ij}, and the distance between the cell centers is $|\mathbf{x}_i - \mathbf{x}_j|$. Note that we assumed here an orthogonal mesh. Generalization to curvilinear grids can be done as shown in Toth et al. (2008). The diffusion coefficients at the face are obtained by simple averaging of the cell centered diffusion coefficient:

$D_{gij} = (D_{gi} + D_{gj})/2$. The discretization of the diffusion operator at resolution changes is described in Appendix A.

The linear system (66)–(67) can be written in a more compact form as the linearized implicit backward Euler scheme

$$\left(\mathbf{I} - \Delta t \frac{\partial \mathbf{R}}{\partial \mathbf{U}} \right) \Delta \mathbf{U} = \Delta t \mathbf{R}(\mathbf{U}^*), \tag{69}$$

where $\mathbf{U}$ are the $I \times (G + 1)$ state variables B and E_g for all I control volumes, and $\Delta \mathbf{U} = \mathbf{U}^{n+1} - \mathbf{U}^*$. $\mathbf{R}$ is defined by the spatially discretized version of the right hand side of equations (66) and (67). The matrix $\mathbf{A} = \mathbf{I} - \Delta t \partial \mathbf{R}/\partial \mathbf{U}$ is a $I \times I$ block matrix consisting of $(G + 1) \times (G + 1)$ sub-matrices. This matrix $\mathbf{A}$ is in general non-symmetric due to the Planck weight w_g^* in the energy exchange between the radiation and electrons. To solve this system we use Krylov sub-space type iterative solvers, like GMRES (Saad & Schultz 1986) or Bi-CGSTAB (van der Vorst 1992). To accelerate the convergence of the iterative scheme, we use a preconditioner. In the current implementation of CRASH, we use the Block Incomplete Lower-Upper decomposition (BILU) preconditioner, which is applied for each adaptive mesh refinement block independently. For gray radiation diffusion the Planck weight is one and the matrix $\mathbf{A}$ can be proven to be symmetric positive definite (SPD) for commonly used boundary conditions (see for example Edwards (1996)). In that case we can use a preconditioned conjugate gradient (PCG) scheme (see for instance Eisenstat (1981)).

For some verification tests, we can attempt to go second order in time under the assumption of temporally constant coefficients using the Crank-Nicolson scheme

$$\frac{\mathbf{U}^{n+1} - \mathbf{U}^*}{\Delta t} = (1 - \alpha)\mathbf{R}(\mathbf{U}^*) + \alpha \mathbf{R}(\mathbf{U}^{n+1}), \tag{70}$$

with $\alpha = 1/2$. The implicit residual can again be linearized $\mathbf{R}(\mathbf{U}^{n+1}) = \mathbf{R}(\mathbf{U}^*) + (\partial \mathbf{R}/\partial \mathbf{U})^* \Delta \mathbf{U}$ to obtain the linear system of equations

$$\left(\mathbf{I} - \alpha \Delta t \frac{\partial \mathbf{R}}{\partial \mathbf{U}} \right) \Delta \mathbf{U} = \Delta t \mathbf{R}(\mathbf{U}^*). \tag{71}$$

We use the same iterative solvers as for the backward Euler scheme.

Finally, we show how we use the solution ΔB and ΔE_g for $g = 1, \ldots, G$ from the non-conservative equations (66) and (67) to advance the solution of the original equations (58)–(60) and still conserve the total energy. One needs to express the fluxes and energies on the right hand side in the latter equations in terms of B^{n+1} and E_g^{n+1} while still keeping the coefficients frozen. After some algebra we obtain

$$
\begin{aligned}
E_i^{n+1} &= E_i^* + \Delta t \sigma_{ie}''(B^{n+1} - B_i^*), &(72)\\
E_e^{n+1} &= E_e^* + C_{Ve}'(B^{n+1} - B^*), &(73)\\
E_g^{n+1} &= E_g^* + \Delta E_g. &(74)
\end{aligned}
$$

This update conserves the total energy to round-off error. Note that at this final stage, taking too large time step may result in negative ion internal energy E_i^{n+1} if $B^{n+1} \ll B_i^*$ and negative electron internal energy E_e^{n+1} if $B^{n+1} \ll B^*$. If this happens, the advance might be redone with a smaller time step, to limit the drop in B, or by some other timestep control scheme. A generalization of the conservative update to the Crank-Nicolson scheme is also implemented for verification tests with time constant coefficients.

For completeness, we mention that in the absence of radiation we solve during the implicit step for the temperatures T_e and T_i instead of the radiation energy-like variables aT_e^4 and aT_i^4. In that case the

corresponding matrix $\mathbf{A}$ is always SPD. In principle, the formulation in temperatures can be generalized to radiation as well. In Landau & Lifshitz (1980), a spectral temperature $T_\nu(E_\nu, \nu)$ is defined, such that the spectral energy density is locally equal to the spectral Planckian energy density at the temperature T_ν: $E_\nu = B_\nu(T_\nu, \nu)$. This relationship is a one-to-one map. A group temperature, T_g, can also be introduced as the discrete analog such that the group energy density can be obtained by

$$E_g(T_g) = \int_{\nu_{g-1/2}}^{\nu_{g+1/2}} B_\nu(T_g, \nu) d\nu. \tag{75}$$

The equation (60) can be recast as equation for the group temperature T_g. This introduces the group specific heat of the radiation $C_g = dE_g/dT_g$. The set of equations (58)–(60) reformulated as an implicit backward Euler scheme for the temperatures T_i, T_e, and T_g can in a similar way as in Edwards (1996) be proven to be SPD. While this scheme has the advantage of being SPD, the conservative update of the group energy density $E_g^{n+1} = E_g^* + C_g^* \Delta T_g$ might result in negative energy density E_g^{n+1} for too large time steps.

3.3.2. Decoupled Implicit Scheme

The coupled implicit scheme of Section 3.3.1 requires the solution of a large system of equations ($G+1$ variables per mesh cell). The preconditioning for such a system can be computationally expensive and requires overall lots of memory. We therefore also implemented a decoupled implicit scheme that solves each equation independently.

For some applications, the electron temperature does not change much due to energy exchange with the radiation. This is typically so if the electrons have a much larger energy density than the radiation, so that T_e changes little due to the interaction with the radiation in a single time step. In that case, we solve first for the electron and ion temperatures without the contributions from the radiation-electron energy exchange. Let again time level $*$ indicate the state after the hydro update and frequency advection, and freeze again C_e^*, D_g^*, σ_{ie}^*, σ_g^* at time level $*$. Discretization in time now leads to

$$\frac{E_i^{n+1} - E_i^*}{\Delta t} = \sigma_{ie}^*(T_e^{**} - T_i^{n+1}), \tag{76}$$

$$\frac{E_e^{**} - E_e^*}{\Delta t} = \sigma_{ie}^*(T_i^{n+1} - T_e^{**}) + \nabla \cdot C_e^* \nabla T_e^{**}, \tag{77}$$

where the time level $**$ of E_e indicates that we still have to do an extra update to time level $n+1$ with the radiation-electron energy exchange. Each radiation group energy density is solved independently using time level $*$ for the electron temperature in B_g^*:

$$\frac{E_g^{n+1} - E_g^*}{\Delta t} = \sigma_g^*(B_g^* - E_g^{n+1}) + \nabla \cdot D_g^* \nabla E_g^{n+1}, \tag{78}$$

where we have exploited the assumption that B_g^* is not stiff.

Equations (76)–(78) can be recast in equations for the $G+1$ independent changes $\Delta B = B^{**} - B^*$ and $\Delta E_g = E_g^{n+1} - E_g^*$:

$$\left[\frac{C'_{Ve}}{\Delta t} + \sigma_{ie}'' - \nabla \cdot C_e' \nabla\right] \Delta B = \sigma_{ie}''(B_i^* - B^*) + \nabla \cdot C_e' \nabla B^*, \tag{79}$$

$$\left[\frac{1}{\Delta t} + \sigma_g^* - \nabla \cdot D_g^* \nabla\right] \Delta E_g = \sigma_g^*(w_g^* B^* - E_g^*) + \nabla \cdot D_g^* \nabla E_g^*. \tag{80}$$

where we have used the definitions (61), (63), and (65) of the coefficients, frozen at time level $*$. Each equation for the changes is in the form of the linearized implicit backward Euler scheme (69) and can be solved independently with iterative solvers like GMRES and Bi-CGSTAB using a BILU preconditioner. As long as the boundary conditions are such that the matrices are symmetric and positive definite, the preconditioned conjugate gradient method might also be used.

In a similar manner as with the coupled implicit scheme, a conservative update for the energy densities can be derived as

$$E_g^{n+1} = E_g^* + \Delta E_g, \tag{81}$$

$$E_i^{n+1} = E_i^* + \Delta t \sigma_{ie}''(B^{**} - B_i^*), \tag{82}$$

$$E_e^{n+1} = E_e^* + C_{Ve}'(B^{**} - B^*) + \Delta t \sum_{g=1}^{G} \sigma_g^*(E_g^{n+1} - w_g^* B^*), \tag{83}$$

that preserve the total energy to roud-off errors. The main difference between the conservative update in the coupled and decoupled schemes is that here the energy exchange between the radiation and electrons is added afterwards as the last term in equation (83).

This scheme requires less computational time for preconditioning and the Krylov solver than the coupled implicit algorithm, however it generally needs more message passing in parallel computations. It is therefore not always guaranteed that the decoupled scheme is faster. The memory usage is always smaller.

3.4. Boundary Conditions

The CRASH code allows for any user specified type of boundary conditions. Several commonly used boundary conditions are readily available in the main code for convenience, e.g., fixed, extrapolation with zero gradient, periodic, and reflective boundary conditions.

For the radiation field, we have implemented a zero or fixed incoming flux boundary condition that is used instead of the extrapolation with zero gradient. This type of boundary condition is useful if there are no sources of radiation outside the computational domain and we assume that outflowing radiation does not return back into the computational domain (zero albedo). Note that simple extrapolation with zero gradient can make the radiation diffusion problem ill-posed. The boundary condition is derived as follows: Radiation diffusion approximation corresponds to a linear-in-angle intensity distribution

$$I_g = \frac{c}{4\pi} E_g + \frac{3}{4\pi} \mathbf{F}_g \cdot \mathbf{n}, \tag{84}$$

so we can calculate the radiation flux through a boundary surface. If we define the outward pointing normal vector of the boundary as $\mathbf{n}_b$, the net flux of radiation energy inward through this boundary is

$$F_g^{\mathrm{in}} = -\int_{\mathbf{n}\cdot\mathbf{n}_b<0} \mathbf{n}_b \cdot \mathbf{n} I_g d\Omega = \frac{cE_g}{4} - \frac{1}{2}\mathbf{n}_b \cdot \mathbf{F}_g, \tag{85}$$

where the closure (84) is used. In the radiation diffusion model, the flux is written as $\mathbf{F}_g = -D_g \nabla E_g$, where the diffusion coefficient D_g is a nonlinear function of E_g and ∇E_g in a flux limited diffusion model. The boundary condition satisfies

$$E_g + \frac{2D_g}{c}\mathbf{n}_b \cdot \nabla E_g = \frac{4}{c}F_g^{in}. \tag{86}$$

For the left boundary in the x-direction, for instance, this can be discretized as

$$\frac{E_{g0} + E_{g1}}{2} - \frac{2D_g}{c}\frac{E_{g1} - E_{g0}}{\Delta x} = \frac{4}{c}F_g^{in}, \tag{87}$$

where the index 1 corresponds to the last physical cell and 0 to the ghost cell. This equation can be solved for the ghost cell value. For zero incoming radiation flux boundary conditions we set $F_g^{in} = 0$.

4. CODE VERIFICATION

To test the CRASH as well as the BATS-R-US and SWMF codes, we have implemented numerous tests. These tests are subdivided in two categories: functionality tests and verification tests. Both test suites are performed automatically and return pass or fail messages depending on whether or not certain predefined tolerance criteria are met. This automated testing process provides a software quality confidence especially when used in combination with a software version control system like CVS (Concurrent Versions System) to recover previous correctly performing code.

The functionality tests are performed nightly on several computer platforms with different compilers and number of processors. They consist of unit tests and full system tests. The unit tests are designed to test a particular unit, for example a linear equation solver. The full system tests on the other hand, exercise the code in the way the end-users will use it for their research applications. We always try to cover as much code as possible with these tests so that we can discover bugs and other unwanted side effects early on.

To test the correctness of the implemented algorithms we have also constructed a suite of verification tests. This suite is executed daily on a dedicated parallel computer and runs specific simulations to quantify against analytic and semi-analytic solutions, whenever possible. The CRASH test repository currently covers a wide range of tests for hydrodynamics, multi-material advection methods, gray and multigroup radiation diffusion, heat conduction, to mention a few. These are performed to test for grid and/or time convergence, as deemed necessary. We also simulate full system laboratory experiment configurations in various geometries, dimensionality, and physics fidelity. The results are either validated against laboratory experiments or simply used to check that the code keeps performing these simulations as expected. Once a week, we also perform a parallel scalability test on a large parallel computer to verify that the code does not degrade in performance during further development of the software.

In the following sub-sections, we highlight some specific verification tests related to the implicit radiation (Section 4.2) and heat conduction (Section 4.3) solver. The tests cover both Cartesian and rz-geometry, and some of them also involve the hydrodynamic solver. We demonstrate a 3D full system test in Section 4.4 and describe the parallel scalability in Section 4.5.

4.1. Error Assessment

For the assessment of the accuracy of the solutions in the test suites, an appropriate definition of the numerical errors have to be defined. We will use two types of errors to quantify the verification analysis: The relative L1 error is defined as

$$E_{\text{L1}} = \sum_{\alpha=1}^{N} \frac{\sum_{i=1}^{I} |\mathbf{U}_{\alpha i} - \mathbf{V}_{\alpha i}|}{\sum_{i=1}^{I} |\mathbf{V}_{\alpha i}|}, \tag{88}$$

where $\alpha = 1, \ldots, N$ indexes the state variables of numerical solution vector $\mathbf{U}$ and the reference solution $\mathbf{V}$, and $i = 1, \ldots, I$ indexes the grid cells of the entire computational domain. For test problems with smooth solutions, we will also use the relative maximum error defined by

$$E_{\mathrm{L}\infty} = \sum_{\alpha=1}^{N} \frac{\max_{i=1,\ldots,I} |\mathbf{U}_{\alpha i} - \mathbf{V}_{\alpha i}|}{\max_{i=1,\ldots,I} |\mathbf{V}_{\alpha i}|}. \tag{89}$$

Quite often the reference solution is defined on a grid with higher resolution than that of the numerical solution. In that case, we first coarsen the reference solution to the resolution of the numerical solution.

4.2. Radiation Tests

4.2.1. Su-Olson Test

Su & Olson (1996) developed a one-dimensional Marshak wave test, to check the accuracy of the scheme and the correctness of the implementation of the time-dependent non-equilibrium gray radiation diffusion model. In this test, radiation propagates through a cold medium that is initially in absence of radiation. The equations are linearized by the choice of the specific heat of the material $C_V = 4aT^3$ as well as by setting the Rosseland and Planck opacities to the same uniform and time-independent constant $\kappa_R = \kappa_P = \kappa$. The cold medium is defined on a half-space of the slab geometry $0 \leq x < \infty$. At the boundary on the left, a radiative source is specified, creating an incident radiation flux of $F^{in} = aT_{in}^4$, where $T_{in} = 1 \, \mathrm{keV}$. As time progresses, the radiation diffuses through the initially cold medium and by energy exchange between radiation and matter, the material temperature will rise. In Su & Olson (1996), a semi-analytical solution is derived for the time evolution of the radiation energy and material temperature. We will use this solution for this verification test.

For convenience, we locate the right boundary at the finite distance $x = 5$ cm and impose a zero incoming radiation flux on that boundary. We decompose the computational domain in 6 grid blocks at the base level with 10 cells per block. Between $x = 5/6$ cm and $x = 5/3$ cm, the domain is refined by one level of AMR. During the time evolution, the radiation diffuses to the right through the resolution changes. The system is time evolved with the implicit radiation diffusion solver by using a preconditioned conjugate gradient method till the final time 0.02 ns. The solver steps through a series of fixed time steps of 5×10^{-4} ns and we use a Crank-Nicolson approach to achieve second order accurate time-integration. Note that this is possible because coefficients of the matrix to be solved are not time dependent. The computed radiation and material temperatures at the final time are shown in Figure 1 and agree well with the semi-analytical solution.

Figure 2 shows the relative L1 error of the radiation and material teperatures versus increasing grid resolution of the base level grid. We did not use the semi-analytical solution as the reference, since it is difficult to get an accurate enough solution with the quadrature method as mentioned by Su & Olson (1996). Instead, we use a very high resolution (1920 cells) numerical reference solution obtained with the CRASH code. Four different base level resolutions with 60, 120, 240, and 480 cells are used to demonstrate the second order convergence. The time step is proportional to the cell size Δx.

4.2.2. Lowrie's Non-equilibrium Radhydro Solutions

Lowrie & Edwards (2008) designed several shock tube problems for the non-equilibrium gray radiation diffusion coupled to the hydrodynamic equations that can be used for code verification. These solutions are planar radiative shock waves where the material and radiation temperatures are out of equilibrium near the shock, but far from the shock the flow is assumed to be in radiative equilibrium. Depending on the Mach number of the pre-shock state, a wide range of shock behavior can occur. For the CRASH test suite, we selected a few of the semi-analytic solutions from Lowrie & Edwards (2008). In this section we will describe the Mach 1.05 flow with uniform opacities as an example. Here the shock is smoothed out by the energy exchange with the diffusive radiation. Another more challenging Mach 5 problem with non-uniform opacities will be described in Section 4.3.3.

The Mach 1.05 test is performed on a 2D non-uniform grid. The initial condition is taken to be the same as the original steady state reference solution. Since the system of equations is Galilean invariant, we can add an additional velocity -1.05 so that the velocity on the left boundary is zero while the smoothed shock will now move to the left. This new initial condition as well as the velocity vector are rotated by $\tan^{-1}(1/2) \approx 26.56°$. This means that there is a translational symmetry in the $(-1, 2)$ direction of the xy-plane as shown in Figure 3. The computational domain is $-0.12 < x < 0.12$ by $-0.02 < y < 0.02$ decomposed in 3×3 grid blocks of 24×4 cells each. We apply one level of refinement inside the region $-0.04 < x < 0.04$ by $-0.02/3 < y < 0.02/3$. The initial smoothed shock starts at the right boundary of the refined grid and we time evolve the solution till it reaches the resolution change on the left as shown in Figure 3. For the boundary conditions in the x direction we use zero radiation influx conditions for the radiation field, while zero gradient is applied to the remaining state variables. On the y boundaries, we apply a sheared zero gradient in the $(-1, 2)$ direction for all variables.

The hydrodynamic equations are time evolved with the HLLE scheme with a CFL number 0.8. We use the generalized Koren limiter with $\beta = 3/2$ for the slope reconstruction. For the implicit radiation diffusion solver, we use the GMRES iterative solver in combination with a BILU preconditioner. The specific heat is time dependent since it depends on the density, therefore the implicit scheme is only first order accurate in time. To enable second order grid convergence for this smooth test problem, we compensate this by reducing CFL number proportional to the grid cell size, in other words $\Delta t \propto \Delta x^2$, so that second order accuracy with respect to Δx can be achieved. We increase the spatial resolution by each time doubling the number of grid blocks at the base level in both the x and y directions.

The convergence of the numerically obtained material and radiation temperatures along the $y = 0$ cut at the final time $t = 0.07$ is shown in Figure 4. The solid, dotted, and dashed lines correspond to the solutions with the 3×3, 6×6, and 12×12 base level grid blocks, respectively. The advected semi-analytical reference solution is shown as a blue line for comparison.

To assess the order of accuracy, the grid convergence is shown in Figure 5 for the three resolutions. The relative L1 error is calculated using the density, velocity components, and both the material and radiation temperatures. We obtain second order convergence for both the conservative as well as the non-conservative (using the pressure equation instead of the total energy) hydrodynamic schemes. The latter scheme can be used because in the Mach 1.05 test the hydro shock is smoothed out by the interaction with the radiation.

4.2.3. Double Light Front

As a test for the multigroup radiation diffusion model we developed a double light front test problem. This test is used to verify the implementation of both the group diffusion and flux limiters. At the light front the discontinuity in the radiation field switches on the flux limiter. This limiter is used to correct the radiation propagation speed in the optically thin free streaming regime. With the light front test we can then check that we obtain the speed of light propagation of the front and that the front maintains as much as possible the initial discontinuity.

This test is constructed as follows: We use a 1D computational domain of the size of 1 m in the x-direction. On this domain, we initialize the two radiation group energy densities E_g ($g = 1, 2$) with a very small, positive number to avoid division by zero in the flux limiter. Also the Rosseland mean opacities are set to a small number corresponding to strong radiation diffusion, while the Planck mean opacities are set to zero corresponding to an optically thin medium. The radiation energy density of the first group enters from the left boundary by applying a fixed boundary condition with value one in arbitrary units. On the right boundary this group is extrapolated with zero gradient. Note that these are the proper boundary conditions in the free-streaming limit and not the diffusive flux boundary conditions described in Section 3.4. The second radiation group enters from the right boundary with density one, and it is extrapolated with zero gradient at the left boundary. We time evolve both groups for 0.5 m/c seconds. The analytic solution will then be two discontinuities that have reached $x = 0.5$ m, since both fronts propagate with the speed of light c.

The computational domain is non-uniform. In the coarsest resolution there are 10 grid blocks of 4 cells each at the base level. Inside the regions $0.1 < x < 0.2$ and $0.8 < x < 0.9$, we use one level of refinement. The total time evolution is divided into 400 fixed time steps. We use GMRES for the radiation diffusion solver in combination with a BILU preconditioner. For the grid convergence we reduce the fixed time step quadratically with the grid resolution. This time step reduction mimics second order discretization in time. In Figure 6, the two group energy densities are shown for the base level grid resolutions 40, 80, 160, and 320. Clearly, with increasing number of cells, the solution converges towards the reference discontinuous fronts at $x = 0.5$.

In Figure 7, the grid convergence is shown for the four resolutions. The relative L1 error is calculated using both radiation group energy densities and compared to the analytical reference solution with the discontinuities at $x = 0.5$. In Gittings et al. (2008), it was stated that for a second order difference scheme the convergence rate for a contact discontinuity is 2/3. Indeed, we find this type of convergence rate, due to the numerical diffusion of the discontinuities, for the light front test. We have also performed the tests in the y and z directions to further verify the implementation.

4.2.4. Relaxation of Radiation Energy Test

This test is designed to check the relaxation rate between the material and the radiation. The energy exchange between the material and radiation groups can be written as

$$C_V \frac{\partial T}{\partial t} = \sum_{g=1}^{G} \sigma_g (E_g - B_g), \tag{90}$$

$$\frac{\partial E_g}{\partial t} = \sigma_g (B_g - E_g). \tag{91}$$

For a single radiation group, an analytic expression can be found to describe the relaxation in time. However, for arbitrary number of groups, a time dependent analytic solution is less obvious, except for some rather artificial cases. Here we make the assumption of an extremely large value of the specific heat C_V to make the analysis more tractable. In that case, the material temperature is time independent, so that B_g is likewise time independent. The solution is then $E_g = B_g(1 - e^{-\sigma_g t})$ assuming $E_g(t = 0) = 0$ initially. At time $t = 1/\sigma_g$, the group radiation energy density is $E_g = B_g(1 - 1/e)$. Note that this test only needs one computational mesh cell in the spatial domain. We set $T = 1\,\mathrm{keV}$ and the resulting Planckian spectrum, defined by B_g, is depicted by the dotted line in the left panel of Figure 8. We use 80 groups logarithmically distributed over the photon energy domain in the range of $0.1\,\mathrm{eV}$ to $20\,\mathrm{keV}$. The computed E_g at time $t = 1/\sigma_g$ are shown as + points. For the simulation we used the GMRES iterative solver and the Crank-Nicolson scheme. To assess the error, we repeated the test with time steps of $1/20$, $1/40$, and $1/80$ of the simulation time. The second order convergence rate is demonstrated in the right panel of Figure 8.

4.3. Heat Conduction Tests

4.3.1. Uniform Heat Conduction in rz-geometry

This test is designed to verify the implicit heat conduction solver in rz-geometry. It tests the time evolution of the temperature profile using uniform and time independent heat conductivity. In rz-geometry, the equation of the electron temperature for purely heat conductive plasma follows

$$C_{Ve}\frac{\partial T_e}{\partial t} = \frac{1}{r}\frac{\partial}{\partial r}\left(rC_e\frac{\partial T_e}{\partial r}\right) + \frac{\partial}{\partial z}\left(C_e\frac{\partial T_e}{\partial z}\right). \tag{92}$$

We will set the electron specific heat $C_{Ve} = 1$ and assume the electron conductivity C_e to be constant. In that case, a solution can be written as a product of a Gaussian profile in the z-direction and an elevated Bessel function J_0 in the r-direction (Arfken 1985):

$$T_e = T_{\min} + T_0\frac{1}{\sqrt{4\pi C_e t}}e^{-\frac{z^2}{4C_e t}}J_0(br)e^{-b^2 C_e t}, \tag{93}$$

where $b \approx 3.8317$ is the first root of the derivative of $J_0(r)$. We select the following values for the input parameters: $T_{\min} = 3$, $T_0 = 10$, and $C_e = 0.1$ in dimensionless units.

The computational domain is $-3 < z < 3$ and $0 < r < 1$ discretized with 3×3 grid blocks of 30×30 cells each. In the region $-1 < z < 1$ and $1/3 < r < 2/3$, we apply one level of mesh refinement. We impose a symmetry condition for the electron temperature on the axis. On all other boundaries the electron temperature is fixed to the time dependent reference solution. We time evolve this heat conduction problem with a preconditioned conjugate gradient method from time $t = 1$ to the final time at $t = 1.5$. The Crank-Nicolson approach is used to achieve second order accurate time integration.

The initial and final solutions for the electron temperature are shown in Figure 9 in color contour in the rz-plane. The heat conduction has diffused the temperature in time to a more uniform state. The black line indicates the region in which the mesh refinement was applied. The relative maximum error of the numerically obtained electron temperature versus the analytical solution is shown in Figure 10. Here we used the non-uniform grid with base resolutions of 90^2, 180^2, 360^2, and 720^2 cells and set the time step proportional to the cell size to demonstrate a second order convergence rate.

4.3.2. Reinicke Meyer-ter Vehn Test

The Reinicke & Meyer-ter-Vehn (1991) problem tests both the hydrodynamics and the heat conduction implementation. This test generalizes the well-known Sedov–Taylor strong point explosion in single temperature hydrodynamics by including the heat conduction. The heat conductivity is parameterized as a non-linear function of the density and material temperature: $C_e = \rho^a T^b$. We select the spherically symmetric self-similar solution of Reinicke & Meyer-ter-Vehn (1991) with coefficients $a = -2$ and $b = 13/2$ and the adiabatic index is $\gamma = 5/4$. This solution produces, similar to the Sedov–Taylor blast-wave, an expanding shock front through an ambient medium. However, at very high temperatures, thermal heat conduction dominates the fluid flows, so that a thermal front precedes the shock front. With the selected parameters, the heat front is always at twice the distance from the origin of the explosion as is the shock front.

We perform the test in rz-geometry. The computational domain is divided in 200×200 cells. The boundary conditions along the r and z axes are reflective. The two other boundaries, away from explosion, are prescribed by the self-similar solution. The time evolution is numerically performed as follows: For the hydrodynamics we use the HLLE scheme and the generalized Koren limiter with $\beta = 2$ as the slope limiter. The CFL number is set to 0.8. The heat conduction is solved implicitly with the preconditioned conjugate gradient method. The test is initialized with the spherical self-similar solution with the shock front located at the spherical radius 0.225 and the heat front is at 0.45. The simulation is stopped once the shock front has reached 0.45 and the heat front is at 0.9.

A 1D slice along the r-axis of the solution at the final time is shown in Figure 11. We normalize the output similar to Reinicke & Meyer-ter-Vehn (1991): The temperature is normalized by the central temperature, while the density and radial velocity are normalized by their values of the post-shock state at the shock. The numerical solution obtained by the CRASH code is shown as + symbols and is close to the self-similar reference solution, shown as solid lines. Note that the temperature is smooth due to the heat conduction, except for the discontinuous derivative at the heat front. The wiggle at $r = 0.3$ in the density and radial velocity is a due to the diffusion of the analytical shock discontinuity in the initial condition during the first few time steps. In the left panel of Figure 12, the spherical expansion of temperature at the final time is shown. Clearly, the Cartesian grid with the rz-geometry does not significantly distort the spherical symmetry of the solution. The spatial distribution of the error in the temperature is shown in the right panel. The errors are largest at the discontinuities of the shock and heat fronts as expected.

A grid convergence study is performed with resolutions of 200^2, 400^2, and 800^2 cells. The relative L1 error in Figure 13 is calculated using the density, velocity components, and the material temperature. The convergence rate is first order due to the shock and heat front.

4.3.3. Heat Conduction Version of Lowrie's Test

Any of the verification tests for non-equilibrium gray-diffusion coupled to the single temperature hydrodynamics can be reworked as a test for the hydrodynamic equations for the ions coupled to the electron pressure equation with electron heat conduction and energy exchange between the electrons and ions. As an example, we will transform one of the non-equilibrium gray diffusion tests of Lowrie & Edwards (2008) to verify the heat conduction implementation.

The electron energy density equation (20) without the radiation interaction can be written as

$$\frac{\partial E_e}{\partial t} + \nabla \cdot [E_e \mathbf{u}] + p_e \nabla \cdot \mathbf{u} = \nabla \cdot [C_e \nabla T_e] + \sigma_{ie}(T_i - T_e), \tag{94}$$

where the heat conduction and energy exchange terms on the right hand side depend on the gradients and differences of the temperatures. The equation for the gray radiation energy density (16) on the other hand depends on the gradients and differences of energy densities. By defining the radiation temperature T_r by $E_r = aT_r^4$ and using the definition of the Planckian $B = aT_e^4$, we can rewrite the energy density equation for the radiation as

$$\begin{aligned}
\frac{\partial E_r}{\partial t} + \nabla \cdot [E_r \mathbf{u}] + \frac{1}{3} E_r \nabla \cdot \mathbf{u} &= \nabla \cdot [D_r \nabla E_r] + c\kappa_P(aT^4 - E_r) \\
&= \nabla \cdot [\overline{D}_r \nabla T_r] + c\overline{\kappa}_P(T - T_r),
\end{aligned} \tag{95}$$

where $\overline{D}_r = D_r 4aT_r^3$ and $c\overline{\kappa}_P = c\kappa_P a(T^2 + T_r^2)(T + T_r)$ are the new coefficients that appear due to this transformation. The equations (94) and (95) are now of the same form. To translate a gray diffusion test to a heat conduction test, we reinterpret $\overline{D}_r$ as the heat conductivity C_e and $c\overline{\kappa}_P$ as the relaxation coefficient σ_{ie} in the ion-electron energy exchange. In addition, the material temperature T and radiation temperature T_r have to be reinterpreted as the ion temperature T_i and electron temperature T_e, respectively. Note that we also have to relate the electron pressure and internal energy by $p_e = E_e/3$ similar to the radiation field corresponding to $\gamma_e = 4/3$, and let the electron internal energy and electron specific heat depend on the electron temperature as $E_e = aT_e^4$ and $C_{Ve} = 4aT_e^3$, respectively.

As an example, we transform the Mach 5 non-equilibrium gray diffusion shock tube problem of Lowrie & Edwards (2008). It uses non-uniform opacities that depend on the density and temperature defined by $D_r = 0.0175(\gamma T)^{7/2}/\rho$ and $c\kappa_P = 10^6/D_r$. The above described procedure is used to translate this problem to an electron heat conduction test with energy exchange between the electron and ions. The heat conductivity for this test is $C_e = 4aT_e^3 0.0175(\gamma T_i)^{7/2}/\rho$ and the relaxation coefficient between the electron and ions is $\sigma_{ie} = a(T_i^2 + T_e^2)(T_i + T_e)4aT_e^3 10^6/C_e$.

We perform this Mach 5 heat conduction test on a 2D non-uniform grid. For the initial condition, the 1D semi-analytical steady state reference solution of Lowrie & Edwards (2008) is used. There is a Mach 5 pre-shock flow on the left side of the tube resulting in an embedded hydro shock as well as a steep thermal front (a look at Figure 14 will help to understand this shock tube problem.) We add an additional velocity of Mach -5 so that the pre-shock velocity is zero and the shock is no longer steady, but instead will move to the left with a velocity -5 (in units in which the pre-shock speed of sound is 1). The problem is rotated anti-clockwise on the grid by $\tan^{-1}(1/2)$. The translational symmetry is now in the $(-1, 2)$ direction in the xy-plane similar to the Mach 1.05 shock tube problem described in Section 4.2.2. The computational domain is $-0.0384 < x < 0.0384$ by $-0.0048 < y < 0.0048$. Inside the area $-0.0128 < x < 0.0128$ and $-0.0016 < y < 0.0016$, we apply one level of refinement. This refinement is set up such that both the heat front as well as the shock front will propagate through the resolution change on the left (from fine to coarse) and right (from coarse to fine), respectively. For the boundary conditions in the x-direction, we fix the state on the right side with the semi-analytical solution, but for the left side we use zero gradient. On the y boundaries, we apply a sheared zero gradient in the $(-1, 2)$ direction.

For the evolution till the final time $t = 0.0025$, we use the HLLE scheme together with the generalized Koren limiter with $\beta = 3/2$ to solve the hydrodynamic equations. The CFL number is set to 0.8. The heat conduction and energy exchange between electrons and ions are solved implicitly with the backward Euler scheme using the GMRES iterative solver in combination with a BILU preconditioner.

In Figure 14, the electron (right panel) and ion (left panel) temperatures are shown at the final time along the x-axis. The semi-analytical reference solution is shown as a blue line, while the numerical solution is shown with $+$ symbols for a simulation with 192×24 cells at the base level in the x and y direction. The hydro shock is located near $x \approx 0.0085$ and shows up in the ion temperature as a jump in the temperature, followed directly behind the shock by a strong relaxation due to the energy exchange between the ions and electrons. The electron temperature stays smooth due to strong heat conduction. The heat front is seen with a steep foot at $x \approx -0.022$. This front corresponds to the radiative precursor in the non-equilibirum gray diffusion tests of Lowrie & Edwards (2008). We repeated the test with four different resolutions at the base level: 192×24, 384×48, 768×96, and 1536×192 cells in the x and y direction. The insets in both panels of Figure 14 show the four resolutions as solid, dotted, dashed, dashed-dotted lines, respectively. In the left panel, the zoom-in shows the convergence of the ion temperature towards the embedded hydro shock and the temperature relaxation. In the right panel, the blow-up shows the convergence towards the reference precursor front. Note that no spurious oscillations appear near the shock or near the precursor.

Due to the discontinuity in both the shock and heat precursor, the convergence rate can be at most first order. Indeed, in Figure 15 the relative L1 error shows first order accuracy. The error is calculated using all the density, velocity components and both temperatures. Note that the spike in the ion temperature is spatially so small that a huge number of grid cells are needed to get a fully resolved shock and relaxation state.

4.4. Full System Tests

The CRASH test repository contains a range of full system configurations to be used for validation with future laboratory experiments. In Figure 16, we show the configuration of a 3D elliptic nozzle through which a fast shock of the order of $150\,\mathrm{km/s}$ will be launched, which is still significantly slower than the speed of light. The shock wave is produced by a $1.1\,\mathrm{ns}$ laser pulse from the left with $4\,\mathrm{kJ}$ of energy irradiating a $20\,\mu\mathrm{m}$ thick Beryllium disk, initially located at $x = 0$. A layer of gold is glued to the plastic tube to protect the outside of the tube from the laser-driven shock. The plastic (polyimide) tube is circular for $x < 500\,\mu\mathrm{m}$ with a radius of $600\,\mu\mathrm{m}$. Beyond $x = 750\,\mu\mathrm{m}$ the tube is elliptic by flattening the tube in the y-direction by a factor 2.

The first part of the simulation is performed with the 2D, Lagrangian, radiation hydrodynamic code HYADES (Larsen & Lane 1994) to time advance the laser energy deposition and the response of the system until the end of the laser pulse at $1.1\,\mathrm{ns}$. This laser pulse first shocks and then accelerates the Beryllium to the right. After $1.1\,\mathrm{ns}$ the output of HYADES is used as an initial condition of the CRASH code.

This simulation is performed for a two temperature, electron and ion, plasma. For the radiation, we use the flux limited diffusion approximation with 30 groups. The photon energy is in the range of $0.1\,\mathrm{eV}$ to $20\,\mathrm{keV}$, logarithmically distributed over the groups. Due to the symmetry in the problem we only simulate one quadrant ($y > 0$ and $z > 0$), with reflective boundary conditions at $y = 0$ and $z = 0$. At all other boundaries we use an extrapolation with zero gradient for the plasma and a zero incoming flux boundary for the radiation. The domain size is $[-150, 3900] \times [0, 900] \times [0, 900]$ microns for the x, y, z coordinates. The base level grid consists of $120 \times 20 \times 20$ blocks of $4 \times 4 \times 4$ mesh cells. One level of dynamic mesh refinement is used at material interfaces and the shock front. Overall, the effective resolution is $960 \times 160 \times 160$ cells and there are approximately 4.5 million finite volume cells. The hydrodynamic equations are solved with the HLLE scheme with a CFL number 0.8 together with the generalized Koren limiter with $\beta = 3/2$. The

diffusion and energy exchange of the radiation groups as well as the heat conduction are solved with the decoupled implicit scheme using a Bi-CGSTAB iterative solver. The simulation from 1.1 ns to 13 ns physical time took 1 hour and 55 minutes on 480 cores of the FLUX supercomputer at the University of Michigan.

In Figure 17, we show the shock structure at 13 ns. The accelerated Beryllium compresses the Xenon directly to the right of the interface, which is seen as a high density plasma near $x = 1700 \, \mu$m in the top right panel of Figure 17. This drives a primary shock and the velocity jump at $x \approx 1700 \, \mu$m is seen in the middle left panel. Behind the shock front, the ions are heated as depicted from the middle right panel, followed directly behind the shock by a cooling due to the energy exchange between the ions and electrons. Early on, the electron heating produces ionization and the emission of radiation, and the radiation in turn heat and ionizes the material ahead of the primary shock. The radiation temperature, measuring the total radiation energy density, is shown in the bottom left panel. The photons will interact again with the matter, sometimes after traveling some distance. This is the source of the wall shock seen ahead of the primary shock (Doss et al. 2009, 2011): photons traveling ahead of the shock interact with the plastic wall, heat it, and this in turn drives a shock off the wall into the Xenon. The ablation of the plastic is depicted in the top left panel as a radially inward moving polyimide (in green color) near and even ahead of the primary shock. The compressed Xenon due to the plastic ablation is seen in the top right panel as a faint density feature that is ahead of the primary shock front, between $x = 1700 \, \mu$m and $x = 2000 \, \mu$m. The interaction between the photons and matter is also seen by the radiative precursor to the right of the radiative shock elevating the electron temperature ahead of the shock in the bottom right panel. This is due to the strong coupling between the electrons and radiation field. The reader is referred to Drake et al. (2011) for more details on radiative effects in radiative shock tubes.

4.5. Parallel Performance

We present parallel scaling studies on the Pleiades supercomputer at NASA Ames. This computer is an SGI ICE cluster connected with infiniband. Figure 18 shows the strong scaling for a problem size that is independent of the number of processors. This 3D simulation is a circular tube version of the full system test described in Section 4.4. It uses five materials, 30 radiation groups, and separate electron and ion temperatures. The grid contains $80 \times 8 \times 8$ blocks of $4 \times 4 \times 4$ cells each at the base level and in addition two time dependent refinement levels. There are overall approximately 2.6 million cells in this problem. We use lookup tables for the EOS and opacities, so that the computational time for that is negligible. For the hydrodynamic equations, we use the HLLE scheme together with the generalized Koren limiter with $\beta = 3/2$. The radiation diffusion, electron heat conduction and energy exchange terms are solved implicitly with the decoupled scheme, uing the Bi-CGSTAB iterative solver. This simulation is performed for 20 time steps for the number of cores varying from 128 to 2048, but excludes file I/O to measure the performance of the implicit solver. Up to 1024 cores, we get good scaling. However for more cores we observe saturation in the performance.

5. SUMMARY

We have extended the BATS-R-US code (Powell et al. 1999; Toth et al. 2010) with a new radiation transfer and heat conduction library. This new combination together with the equation-of-state and multigroup opacity solver is called the CRASH code. This code uses the recently developed parallel Block

Adaptive Tree Library (BATL, see Toth et al. (2010)) to enable highly resolved radiation hydrodynamic solutions. The implemented radiation hydrodynamic schemes solve for the gray or multigroup radiation diffusion models in the flux limited diffusion approximation.

In high energy density plasmas, the electrons are most of the time strongly coupled to the ions by collisions. An important exception is at hydrodynamic shocks, where the ions are heated by the shock wave and the electrons and ions are out of temperature equilibrium. Since radiative shocks are the main application for CRASH, we have implemented a separate electron pressure equation with the electron thermal heat conduction. For the electron heat conduction, we have added the option of a flux limiter to limit the thermal flux with the free-streaming heat flux.

The multi-material radiation hydrodynamic equations are solved with an operator split method that consists of three substeps: (1) solving the hydrodynamic equations with standard finite volume shock-capturing schemes, (2) the linear advection of the radiation in frequency-logarithm space, and (3) the implicit solution of the radiation, heat conduction, and energy exchanges. For the implicit solver, standard Krylov solvers are used together with a Block Incomplete Lower-Upper decomposition (BILU) preconditioner. This preconditioner scales well up to 500 or 1000 processors. For future work, we may explore for the implicit multigroup diffusion a multi-level preconditioner to better scale the radiation solver beyond 1000 processors.

We have presented a suite of verification tests that benchmark the performance. These tests verify the correctness and accuracy of the implementation for the gray and multigroup radiation diffusion algorithm and the heat conduction in 1D, 2D, and 3D slab and 2D rz geometry. To demonstrate the full capability of the implementation, we have presented a 3D multi-material simulation of a radiative shock wave propagating through an elliptic nozzle. This configuration will be used in future validation studies.

Since this radiation transfer library is an extension of the BATS-R-US code, the implementation is readily available for MHD simulations as well. This allows for validation studies of the radiation MHD implementation using laboratory-astrophysics experiments or for the simulations of astrophysical plasmas.

A.   DISCRETIZATION OF THE DIFFUSION OPERATOR AT RESOLUTION CHANGES

In Sections 3.3.1 and 3.3.2, the diffusion operator is discretized on a uniform mesh with a standard finite volume method in combination with a central difference approximation for the gradient in the flux calculation as in equation (68). The diffusion coefficient that is needed at the face is obtained by simple arithmetic averaging of the left and right cell center diffusion coefficients. The generalization to resolution changes as in Figure 19 is less straightforward. In the following, we will denote the fine cell centers by a and b, the coarse cell center by c. The flux densities at the resolution changes in the direction orthogonal to the interface are denoted by F_1 and F_2 at the fine faces, and F_3 at the coarse face.

In Edwards (1996), a strategy was developed to discretize the diffusion operator on an adaptive mesh in the context of reservoir simulations. The main ingredients of the method are (1) require the continuity of the flux at the resolution change in the strong sense, i.e. $F_1 = F_2 = F_3$, and (2) discretize the gradient

in the diffusion flux by a one-sided difference. An expression was found for the diffusion flux $\mathbf{F} = -D\nabla E$ in which the diffusion coefficient is replaced by a weighted harmonic average of the cell centered values D_a, D_b, D_c. In Gittings et al. (2008), it was argued that this discretization does not properly propagate the self-similar Marshak waves of the radiation diffusion model, unless the cell centered diffusion coefficients are calculated on a common face temperature.

In the code discussed in this paper, we follow a different approach that replaces the harmonic average of the diffusion coefficient in Edwards (1996) by an arithmetic average and obtain for the flux densities normal to the resolution change interface

$$F_1 = F_2 = F_3 = -\frac{2D}{3\Delta x}\left[E_c - (E_a + E_b)/2\right],\tag{A1}$$

where Δx is the fine cell size and the diffusion coefficient at the face is averaged as

$$D_3 = \left[D_c + (D_a + D_b)\right]/3.\tag{A2}$$

We demonstrated with verification tests including those discussed above that this change produces properly propagating radiative precursor and shock fronts. Generalizations to 1D and 3D are straightforward.

B.   RZ-GEOMETRY

Incorporating the rz-geometry in a finite volume formulation is as follows: the radial cell face area and the cell volume must be made proportional to the distance r from the symmetry axis. In addition, the r component of the momentum equation (18) is modified as

$$\frac{\partial \rho u_r}{\partial t} + \nabla \cdot \left[\rho \mathbf{u}u_r + \hat{\mathbf{r}}(p + p_r)\right] = \frac{p + p_r}{r},\tag{B1}$$

where $\hat{\mathbf{r}}$ is the unit vector in the r direction and $u_r = \mathbf{u}\cdot\hat{\mathbf{r}}$. This correction reflects the fact that the pressure term is a gradient, not a divergence.

REFERENCES

Arfken, G. 1985, Mathematical Methods for Physicists, 3rd edition (San Diego, CA: Academic Press)

Baek, S., Di Matteo, P., Semelin, B., Combes, F., & Revaz, Y. 2009, A&A, 495, 389

Barton, R.T. 1985, in Numerical Astrophysics, eds by J.M. Centrella, J.M. LeBlanc, & R.L. Bowers (Jones and Bartlett, Boston), 482

Buchler, J.R. 1983, J. Quant. Spec. Radiat. Transf., 30, 395

Doss, F.W., Robey, H.F., Drake, R.P., & Kuranz, C.C. 2009, Phys. Plasmas, 16, 112705

Doss, F.W., Drake, R.P., & Myra, E.S. 2011, Phys. Plasmas, submitted

Drake, R.P. 2006, High-Energy Density Physics (Berlin-Heidelberg-NY: Springer)

Drake, R.P. et al. 2011, submitted to High Energy Density Physics

Edwards, M.G. 1996, J. Comp. Phys, 126, 356

Einfeldt, B., Munz, C.D., Roe, P.L., & Sjögreen, B. 1991, J. Comp. Phys., 92, 273

Eisenstat, S.C. 1981, SIAM J. Sci. and Stat. Comput., 2, 1

Gittings, M. et al. 2008, Comput. Sci. Disc, 1, 015005

Godunov, S.K. 1959, Mat. Sbornik, 47, 271

Harten, A., Lax, P.D., & van Leer, B. 1983, SIAM Rev., 25 (1), 35

Koren, B. 1993, in Numerical Methods for Advection-Diffusion Problems, eds C.B. Vreugdenhil & B. Koren (Braunschweig: Vieweg), 117

Landau, L.D. & Lifshitz, E.M. 1980, Theoretical Physics, Vol. 5. Statistical Physics, Part 1. 3rd Edition (Pergamon Press: NY)

Larsen, J. & Lane, S. 1994, J. Quant. Spec. Radiat. Transf., 51, 179

Levermore, C.D. & Pomraning, G.C. 1981, ApJ, 248, 321

Lowrie, R.B. & Edwards, J.D. 2008, Shock Waves, 18, 129

Lund, C.M. & Wilson J.R. 1980, Lawrence Livermore National Laboratory Report UCRL-84678

Marinak, M.M., Kerbel, G.D., Gentile, N.A., Jones, O., Munro, D., Pollaine, S., Dittrich, T.R., & Haan, S.W. 2001, Phys. of Plasmas, 8, 2275

Martínez-Sykora, J., Hansteen, V., De Pontieu, B., & Carlsson, M. 2009, ApJ, 701, 1569

Maselli, A., Ferrara, A., & Gallerani, S. 20009, MNRAS, 395, 1925

Mellema, G., Iliev, I.T., Alvaraz, M.A., & Shapiro, P.R. 2006, New A, 11, 374

Mihalas, D. & Weibel-Mihalas, B. 1984, Foundations of Radiation Hydrodynamics (New York: Oxford Univ. Press)

Minerbo, G.N. 1978, J. Quant. Spec. Radiat. Transf., 20, 451

Morel, J.E. 2000, J. Quant. Spec. Radiat. Transf., 65, 769

Nayakshin, S., Cha, S.H., & Hobbs, A. 2009, MNRAS, 397, 1314

Petkova, M. & Springel, V. 2009, MNRAS, 396, 1383

Pomraming, G.C. 2005, The equations of Radiation Hydrodynamics (Mineola: Dover)

Powell, K.G., Roe, P.L., Linde, T.J., Gombosi, T.I., & DeZeeuw, D.L. 1999, J. Comp. Phys., 154, 284

Reinicke, P., & Meyer-ter-Vehn, J. 191, Phys. Fluids A, 3, 1807

Rijkhorst, E.J., Plewa, T., Dubey, A., & Mellema, G. 2006, A&A, 452, 907

Roe, P.L. 1986, Ann. Rev. Fluid Mech., 18, 337

Saad, Y. & Schultz, M.H. 1986, SIAM J. Sci. Stat. Comput. 7(3), 856

Stein, R.F., Benson, D., & Nordlund, Å2007, in New Solar Physics with Solar-B Mission, eds K. Shibata, S. Nagata, & T. Sakurai, 369, 87

Stone, J.M., Mihalas, D., & Norman, M.L. 1992, ApJS, 80, 819

Su, B. & Olson, G.L. 1996, J. Quant. Spec. Radiat. Transf., 56, 337

Tóth, G. et al. 2005, J. Geophys. Res., 110:A12226, 2005

Tóth, G., Ma, Y., & Gombosi, T.I. 2008, J. Comp. Phys., 227, 6967

Tóth, G. et al. 2010, submitted to J. Comp. Phys.

van der Vorst, H.A. 1992, SIAM J. Sci. and Stat. Comput., 13, 631

Vögler, A., Shelyag, S., Schüssler, M. Cattaneo, F., Emonet, T., & Linde, T. 2005, A&A, 429, 335

Yee, H.C. 1989, NASA TM-101088

Zel'dovich, Ya.B. & Raizer, Yu.P. 2002, Physics of Shock Waves and High-Temperature Hydrodynamic Phenomena (Mineola, NY: Dover Publications)

Table 1. Quantities stored in the EOS tables as a function of $\log T_e$ [eV] and $\log n_a$ $\left[\mathrm{m}^{-3}\right]$.

quantity	stored quantity	units
total pressure p	p/n_a	eV
total internal energy density E	E/n_a	eV
electron pressure p_e	p_e/n_a	eV
electron internal energy density E_e	E_e/n_a	eV
specific heat C_V	$C_V/(n_a k_B)$	
electron specific heat C_{Ve}	$C_{Ve}/(n_a k_B)$	
speed of sound gamma	γ_S	
electron speed of sound gamma	γ_{S_e}	
inverse of ion-electron interaction time	$1/\tau_{ie}$	s^{-1}
electron conductivity	C_e	$\mathrm{J\,m}^{-1}\,\mathrm{s}^{-1}\,\mathrm{K}^{-1}$
mean ionization	$\overline{Z}$	
mean square ionization	$\overline{Z^2}$	

Table 2.   Quantities stored in the opacity tables as a function of $\log \rho \left[\text{kg m}^{-3} \right]$ and $\log T_e$ [eV].

quantity	symbol	units
specific group Rosseland mean opacities	κ_{Rg}/ρ	$\text{kg}^{-1} \, \text{m}^2$
specific group Planck mean opacities	κ_{Pg}/ρ	$\text{kg}^{-1} \, \text{m}^2$
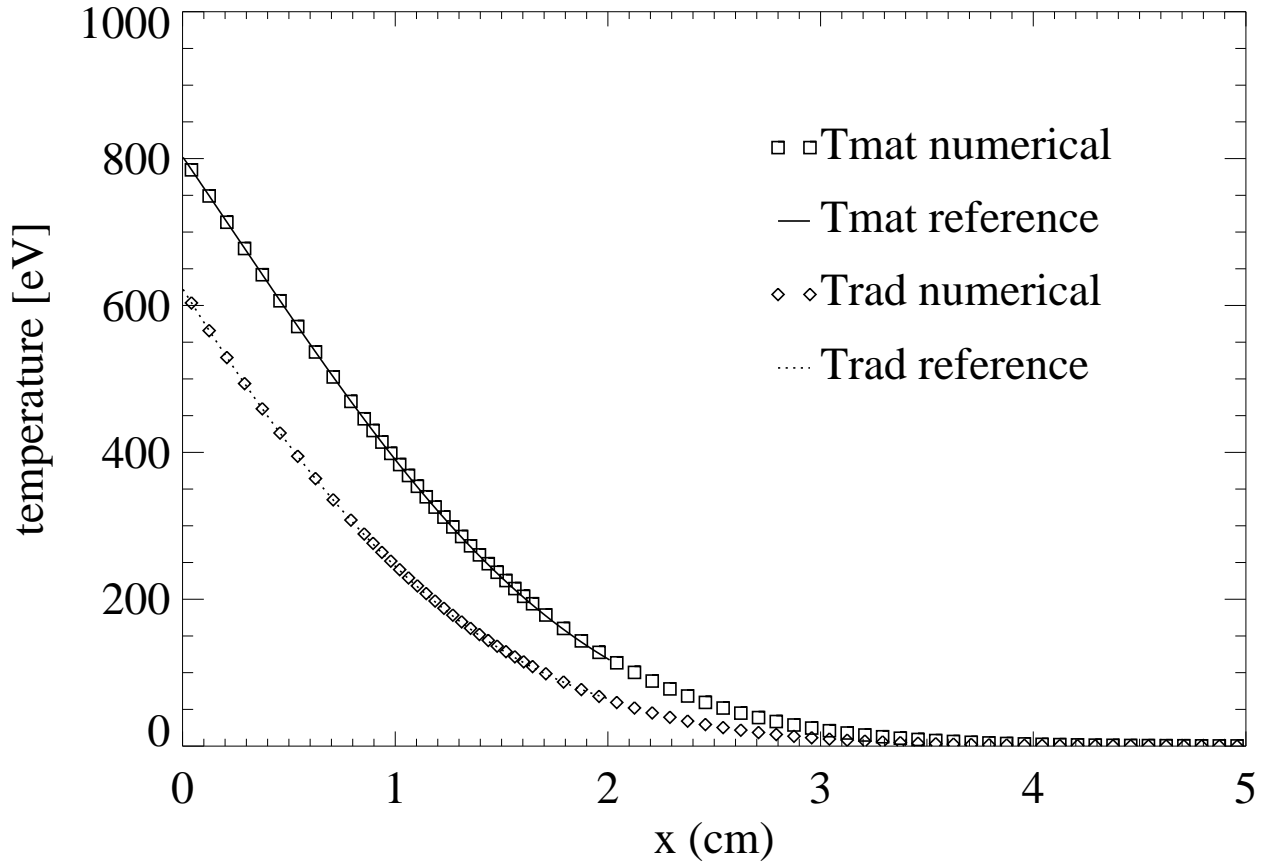
Fig. 1.— The material (T_{mat}) and radiation (T_{rad}) temperature solution of the Su & Olson (1996) non-equilibrium Marshak radiation diffusion problem obtained with the CRASH code on a non-uniform grid. The reference temperatures of the analytical method of Su & Olson (1996) are shown as lines.
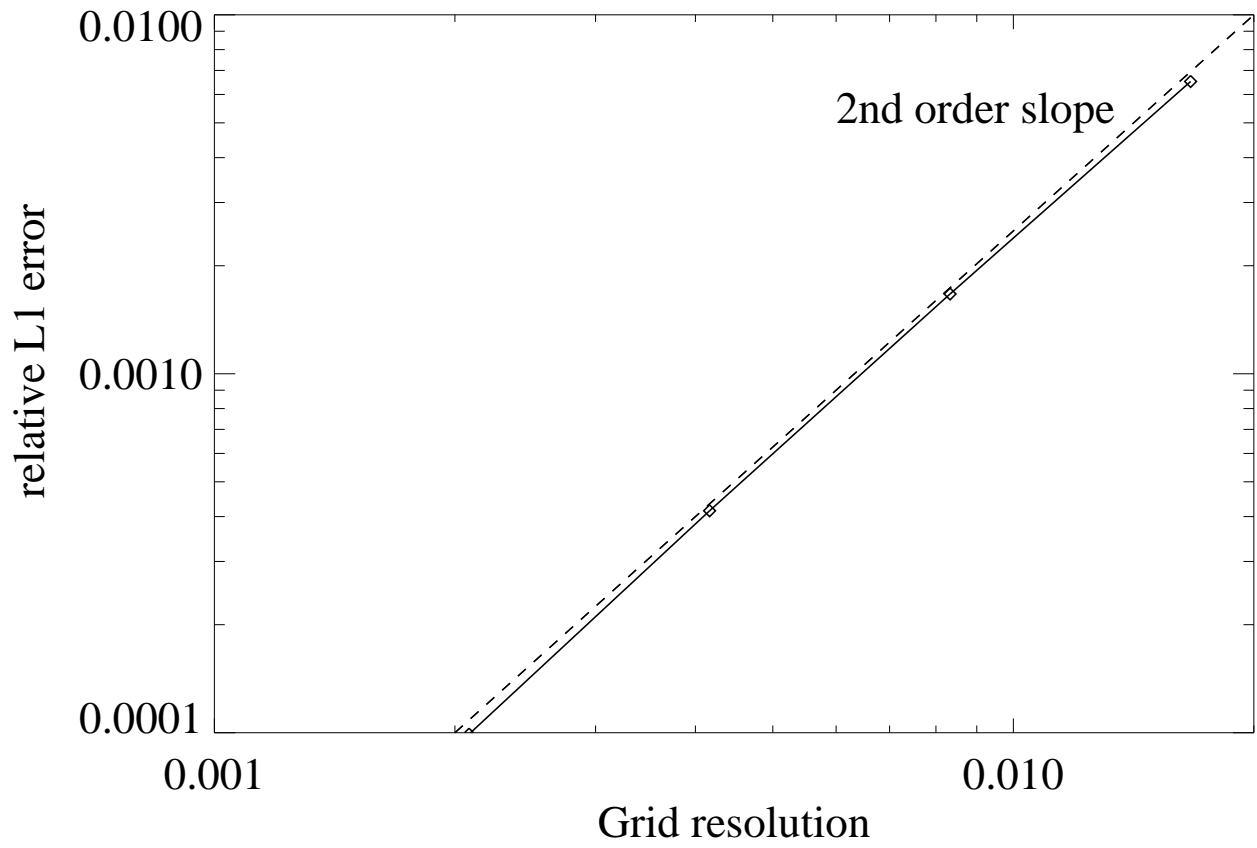
Fig. 2.— The relative L1 error for the Su-Olson test on a non-uniform grid.
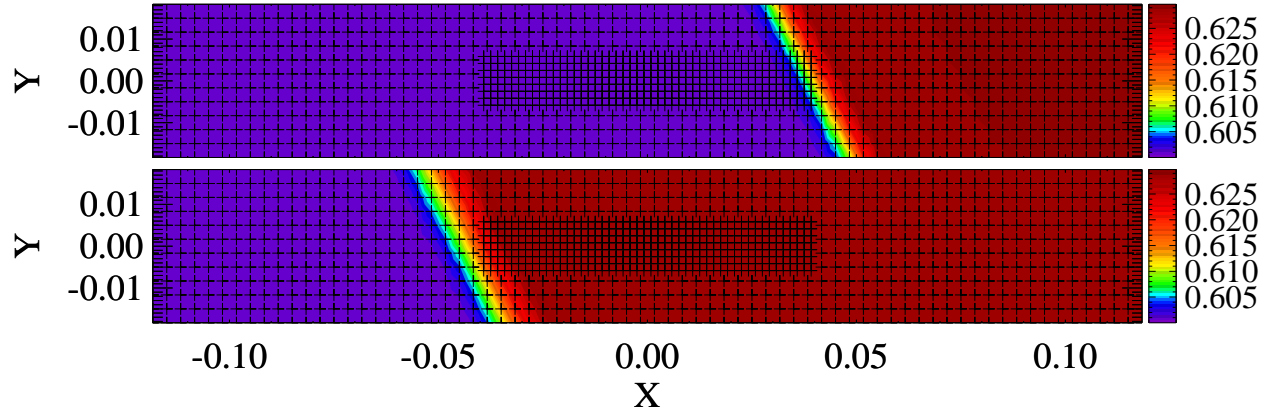
Fig. 3.— Rotated shock tube test on a 2D AMR grid based on the Mach number 1.05 non-equilibrium gray radiation hydrodynamic test in Lowrie & Edwards (2008). Shown is the radiation temperature in color contour at the initial (top panel) and final (bottom panel) times. The black crosses indicate the cell centers.
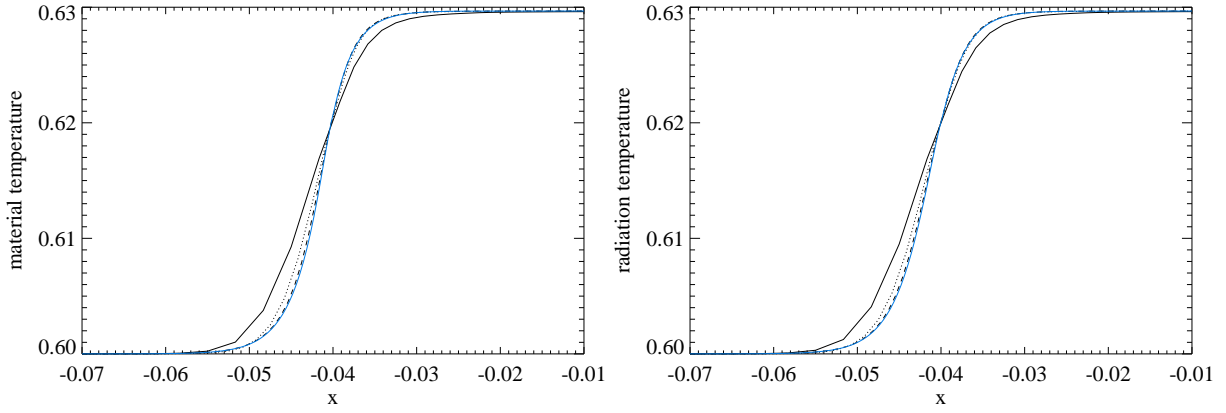
Fig. 4.— The material (left panel) and radiation (right panel) temperatures for the Mach 1.05 radiative shock tube problem at the final time are shown in the x-direction. The solid, dotted, and dashed lines correspond to three different grid resolutions, respectively. The blue line is the semi-analytical reference solution of Lowrie & Edwards (2008).
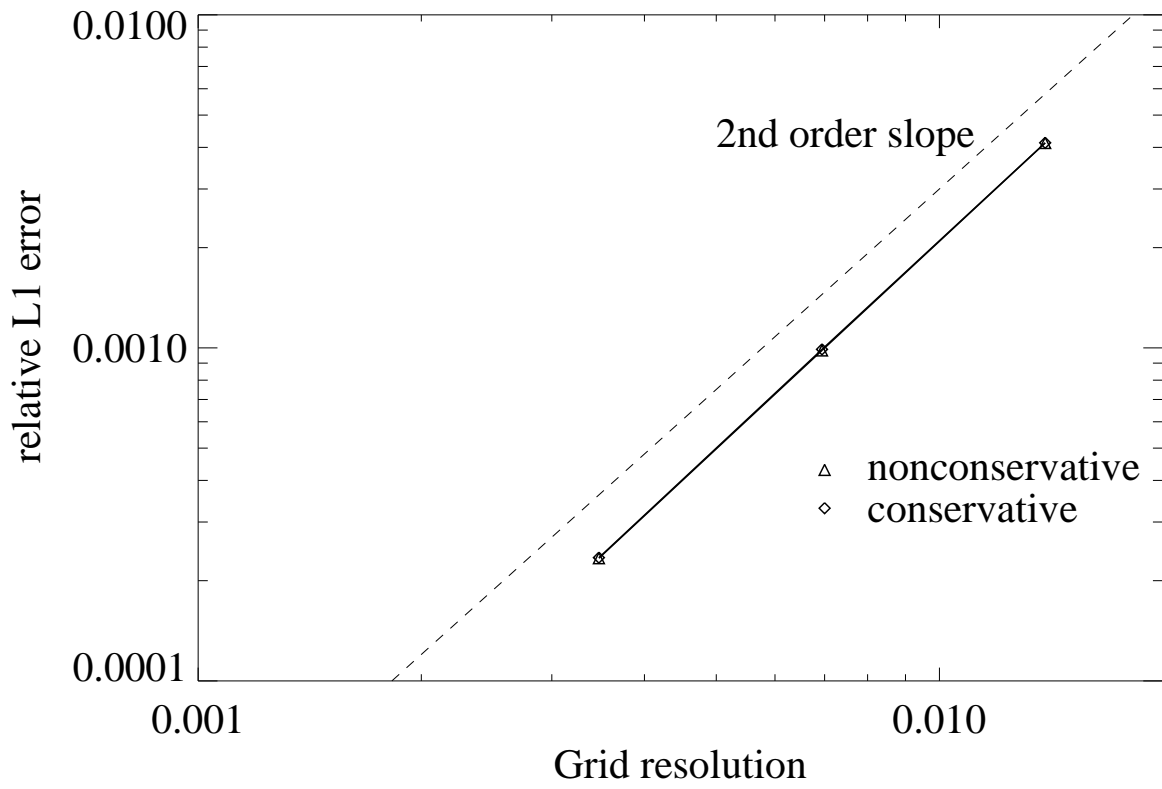
Fig. 5.— The relative L1 error for the Mach 1.05 non-equilibrium radiation diffusion test on a non-uniform grid. Both the non-conservative as well as the conservative hydrodynamic schemes are tested.
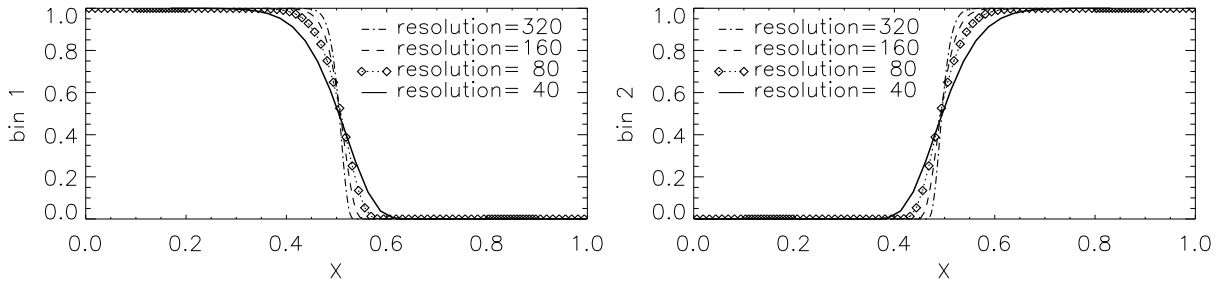
Fig. 6.— Solutions for the 1D double light front test for 4 different non-uniform grid resolutions. The radiation energy for group 1 (left panel) enters from the left boundary, for group 2 (right panel) it enters from the right boundary. The symbols for base resolution 80 shows one level of grid refinement for $0.1 < x < 0.2$ and $0.8 < x < 0.9$.
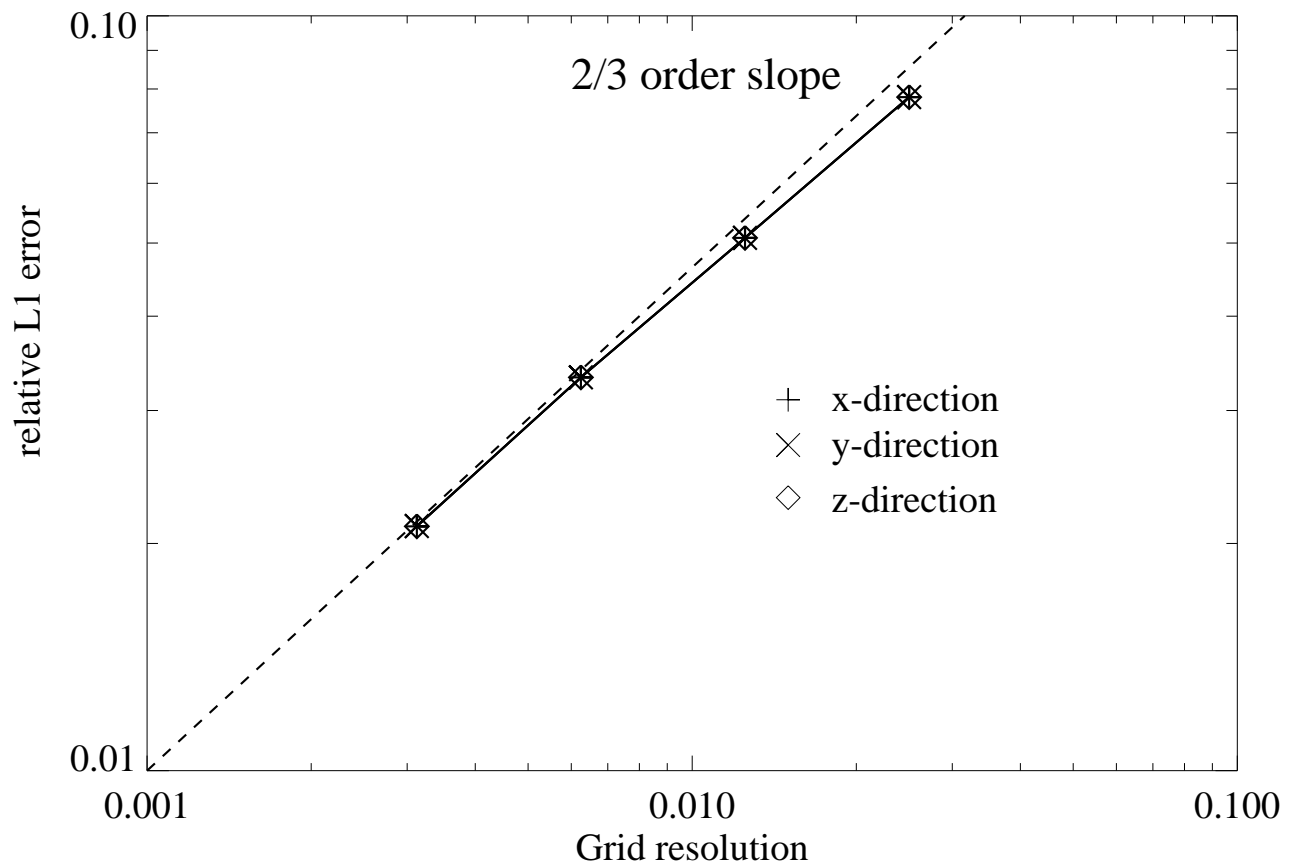
Fig. 7.— Relative L1 error for the double light front test on a non-uniform grid. The test is performed for the x, y, and z directions.
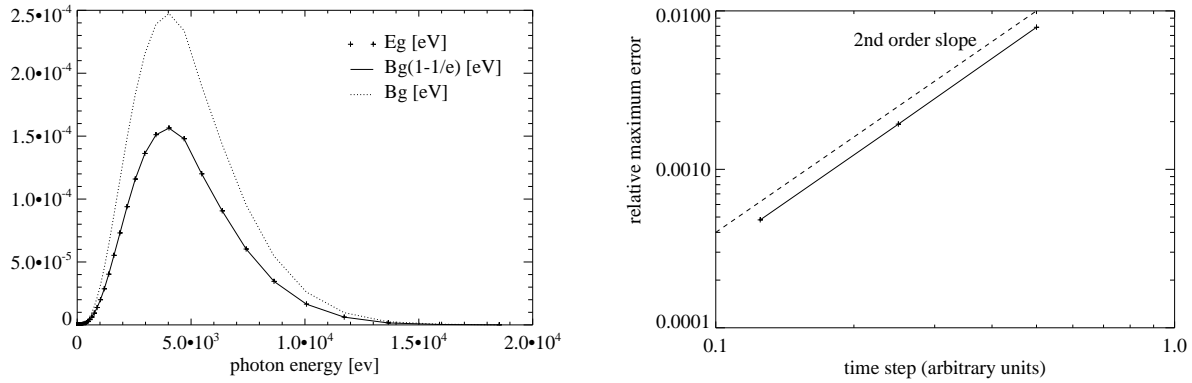
Fig. 8.— The relaxation of radiation energy test for 80 groups. Left panel is for the time independent spectrum B_g (dotted line) and the group radiation energy solution E_g at time $1/\sigma_g$ (+ points) versus the photon energies after 80 time steps. The analytical reference solution is shown as a solid line. Right panel shows the relative maximum error for 20, 40, and 80 time steps demonstrating second order convergence rate.
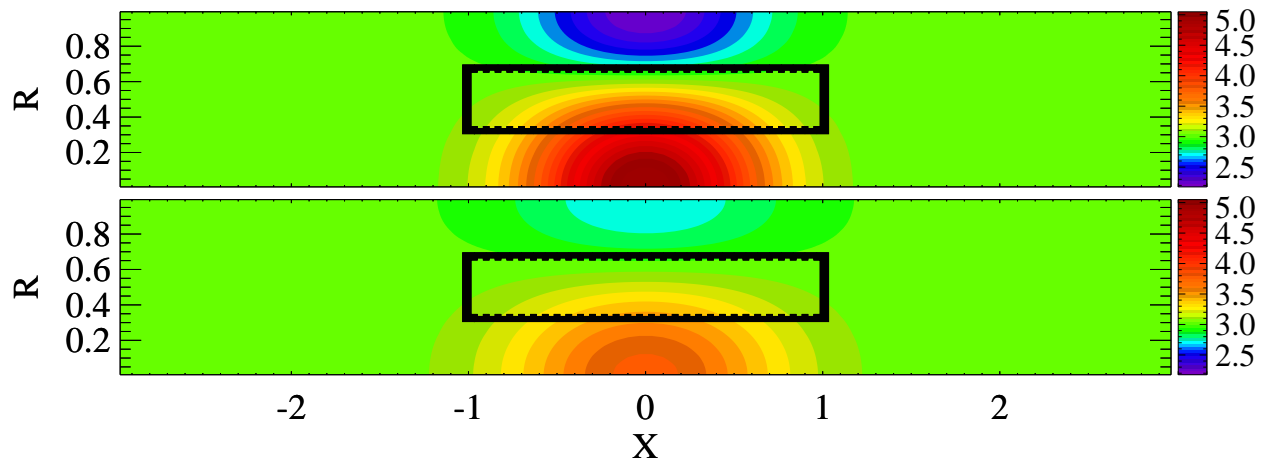
Fig. 9.— The electron temperature for the uniform heat conduction test on a non-uniform grid in *rz*-geometry. The top panel shows the electron temperature in the initial condition while the bottom panel is the electron temperature at the final time. The black box indicates the region within which the grid is refined by one level.
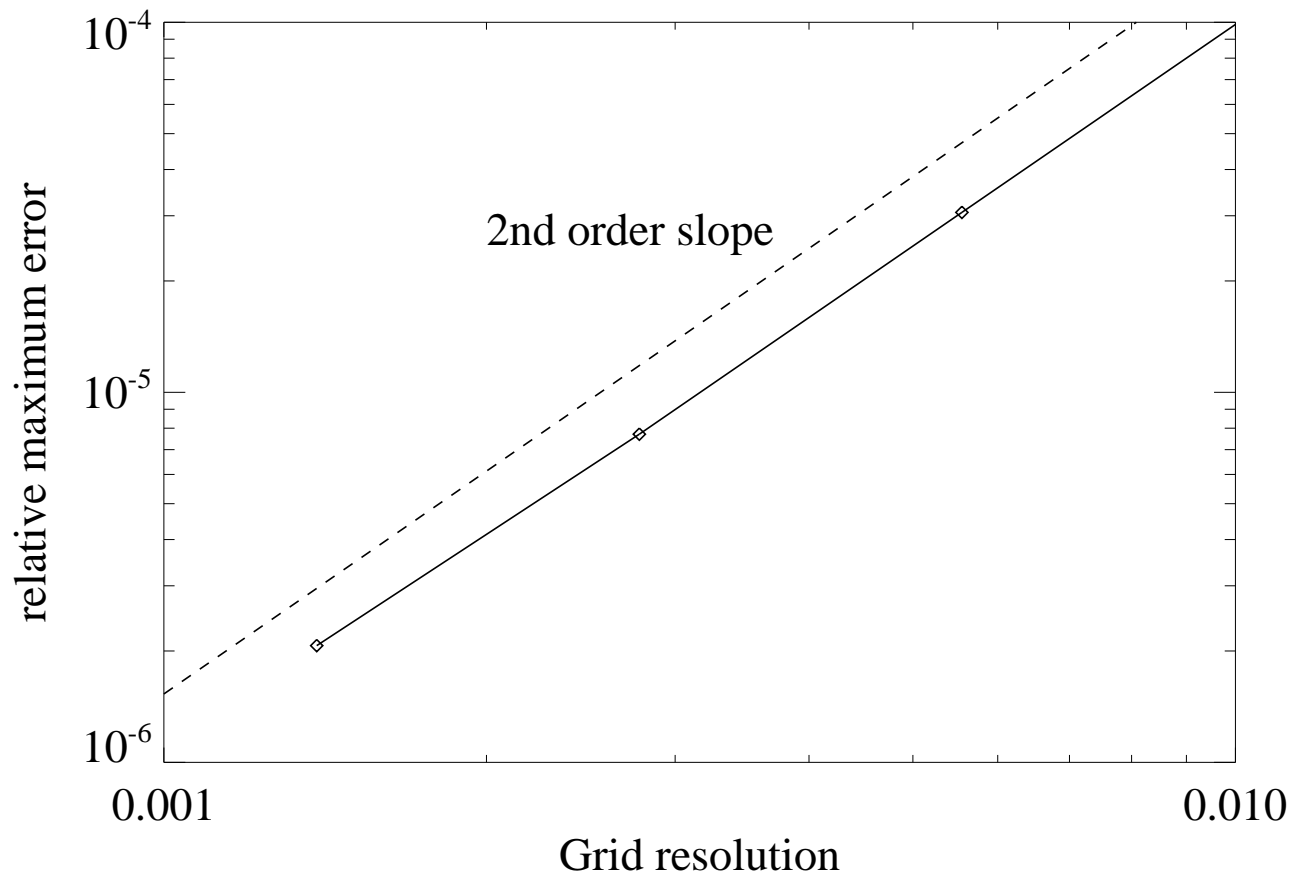
Fig. 10.— The relative maximum error for the uniform heat conduction test on a non-uniform grid in the rz-geometry.
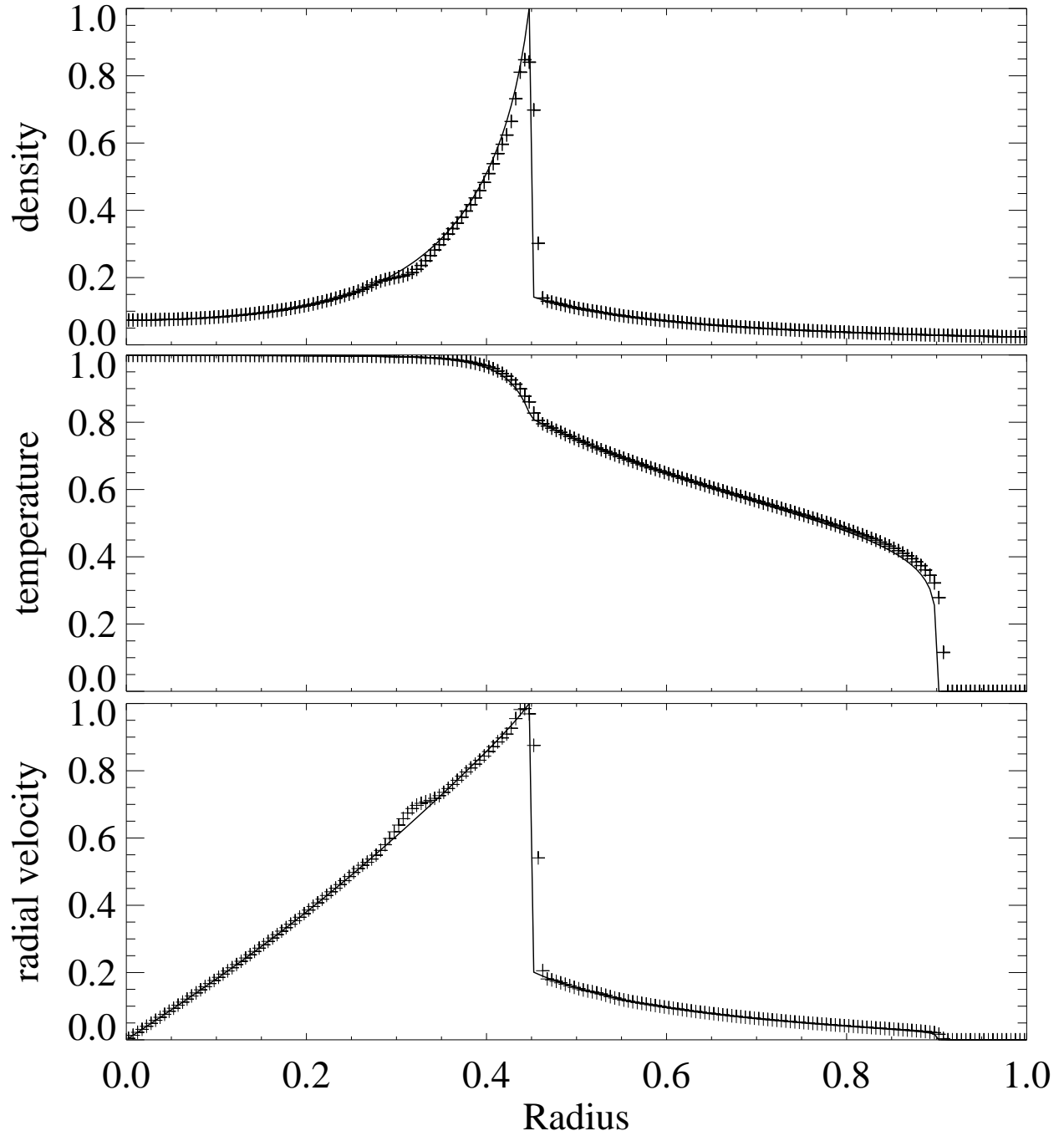
Fig. 11.— Density (top panel), temperature (middle panel), and radial velocity (bottom panel) along the $z = 0$ cut for the Reinicke Meyer-ter Vehn test in rz-geometry. The numerical solution (+ symbols) is at the final time compared to the self-similar analytical reference solution (solid lines).
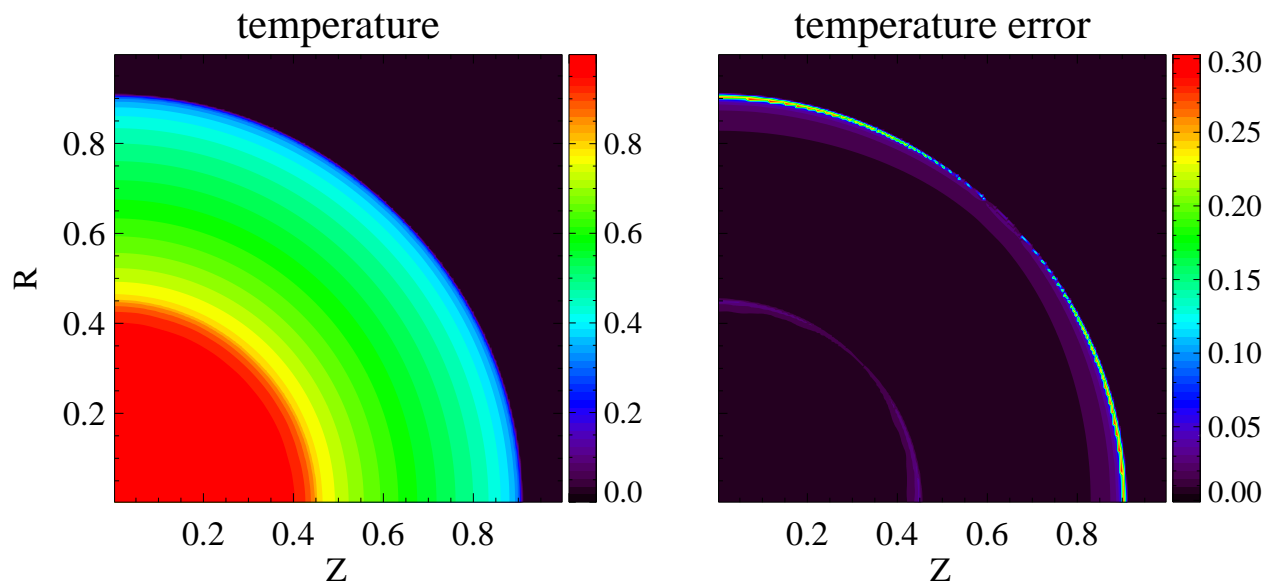
Fig. 12.— The temperature (left panel) and temperature error compared to the reference solution (right panel) for the Reinicke Meyer-ter Vehn test in rz-geometry.
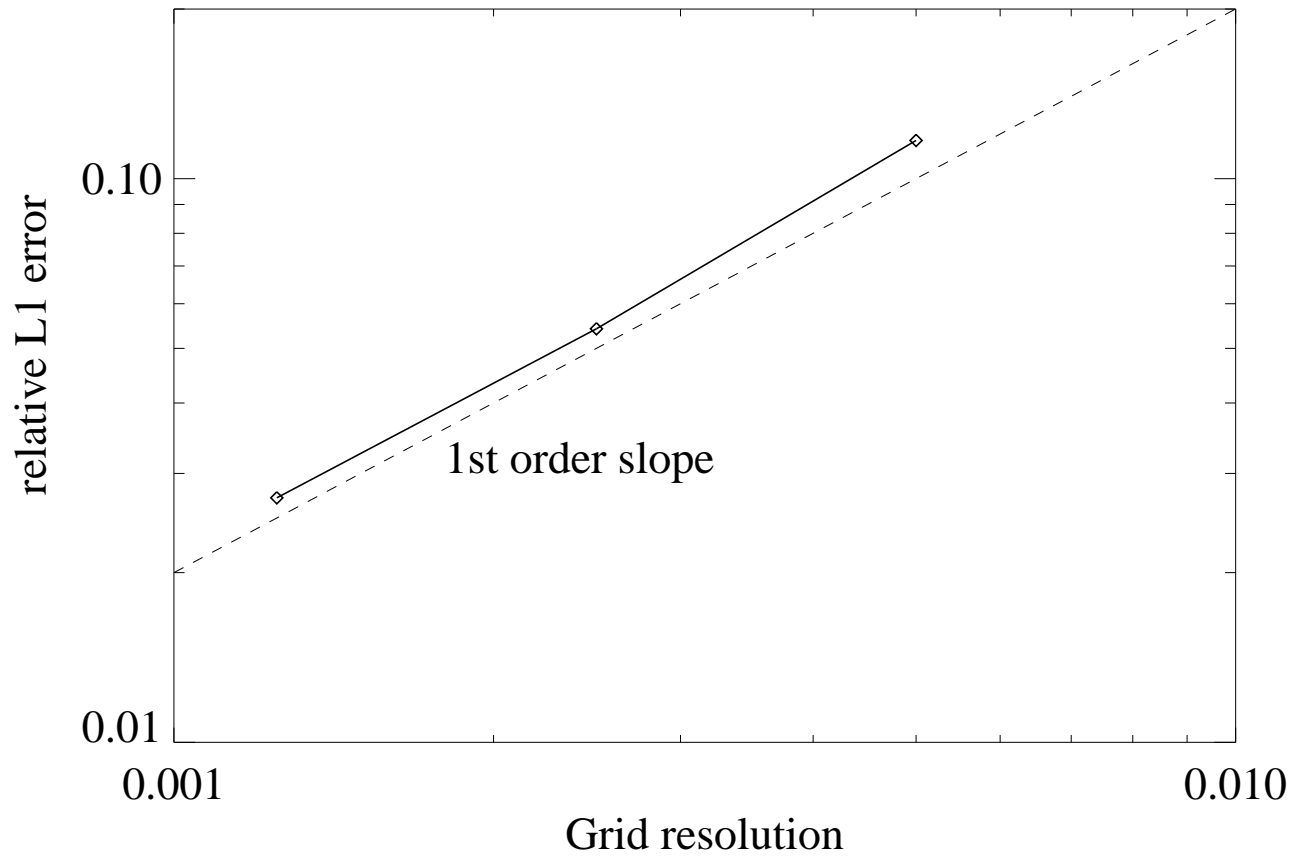
Fig. 13.— The relative L1 error for the Reinicke Meyer-ter Vehn test in rz-geometry.
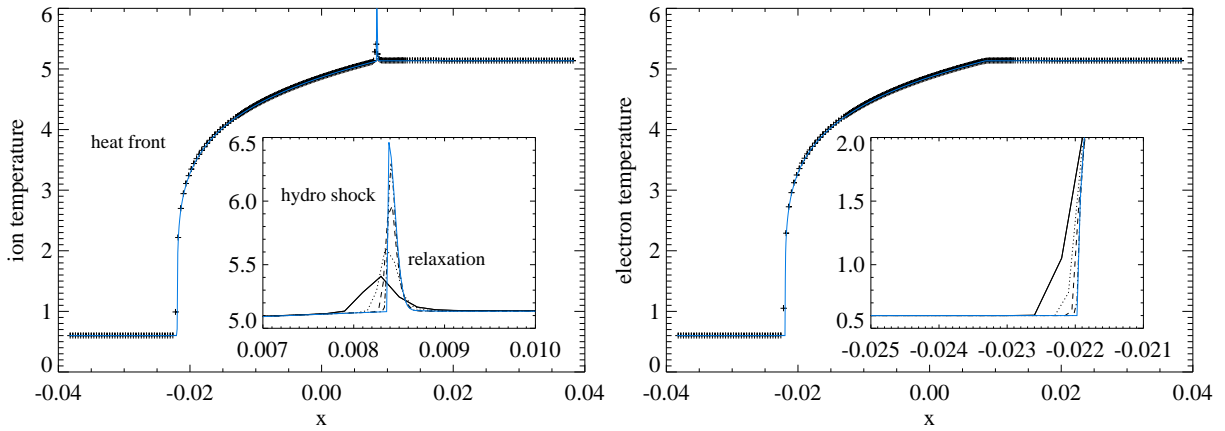
Fig. 14.— Mach 5 shock tube problem of Lowrie & Edwards (2008) transformed to a non-uniform heat conduction and ion-electron collison frequency test and rotated on a 2D non-uniform grid. The ion (left panel) and electron (right panel) temperatures at the final time are shown in the x-direction. The blue line is the reference solution. In the left panel, the grid convergence near the shock is shown in the inset. In the right panel, a blow-up of the grid convergence to the reference heat front is shown.
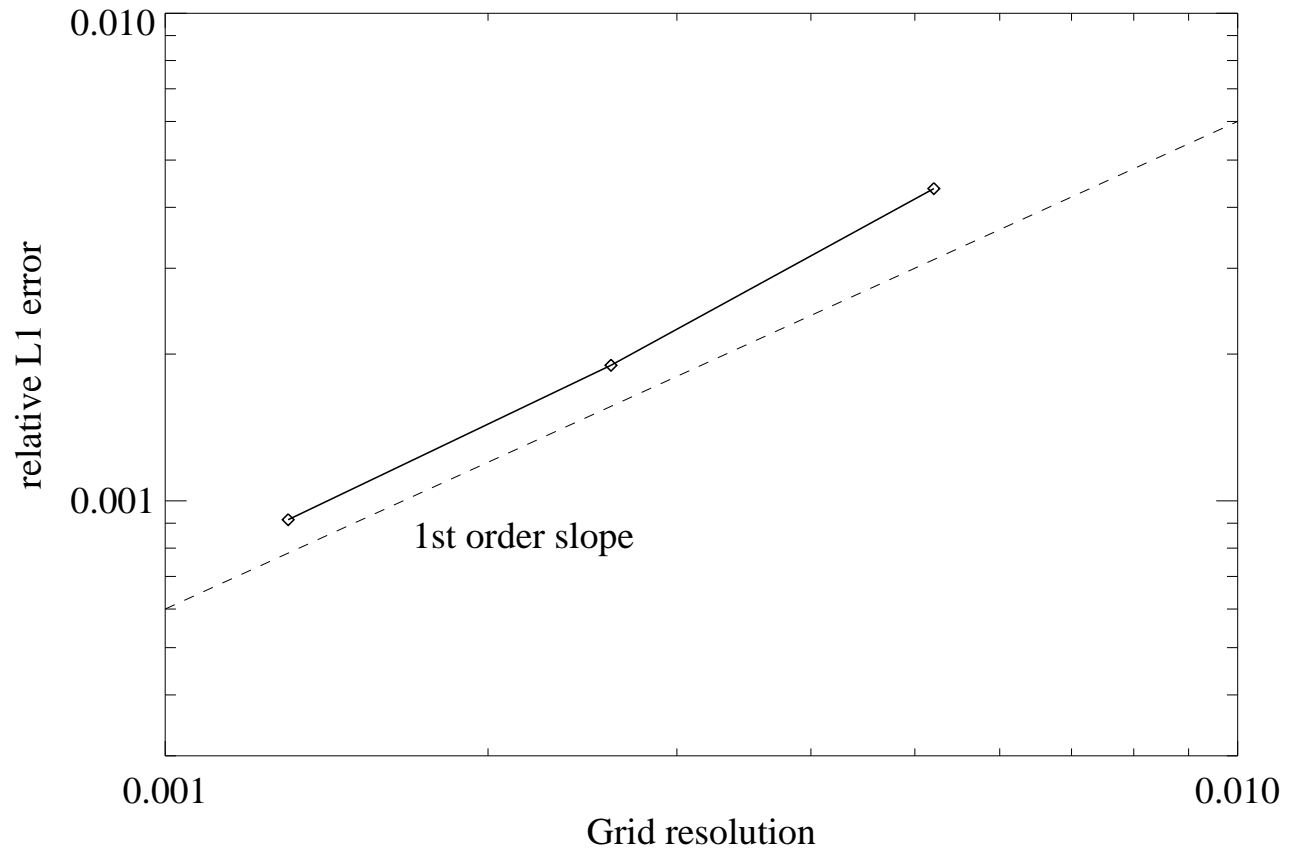
Fig. 15.— Relative L1 error for the Mach 5 non-equilibrium heat conduction test on a non-uniform grid.
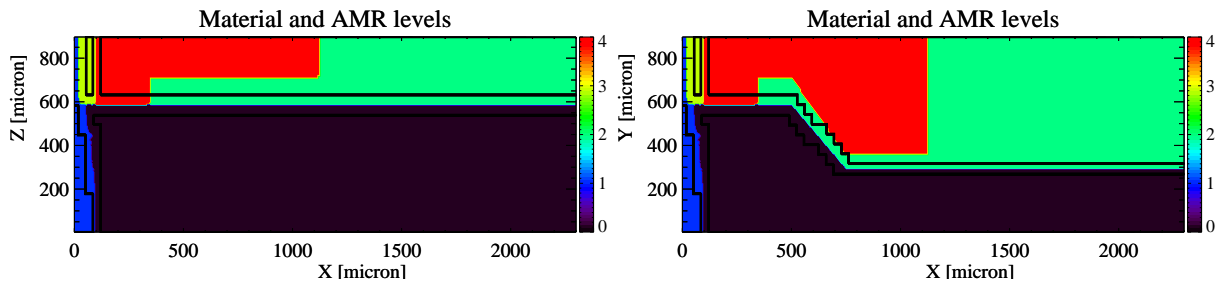
Fig. 16.— The geometry of the 3D elliptic nozzle experiment after 1.1 ns, consisting of 5 materials: Beryllium (blue), Xenon (black), polyimide (green), gold (yellow), and acrylic (red) in both panels. The radius of the inside of the polyimide tube is $600\,\mu$m in the $y = 0$ plane (left panel). In the $z = 0$ plane (right panel), the radius of the inner tube is $600\,\mu$m for $x < 500\,\mu$m, but shrinks to $300\,\mu$m beyond $x = 750\,\mu$m. The lines represent the mesh refinement at material interfaces and shock fronts.
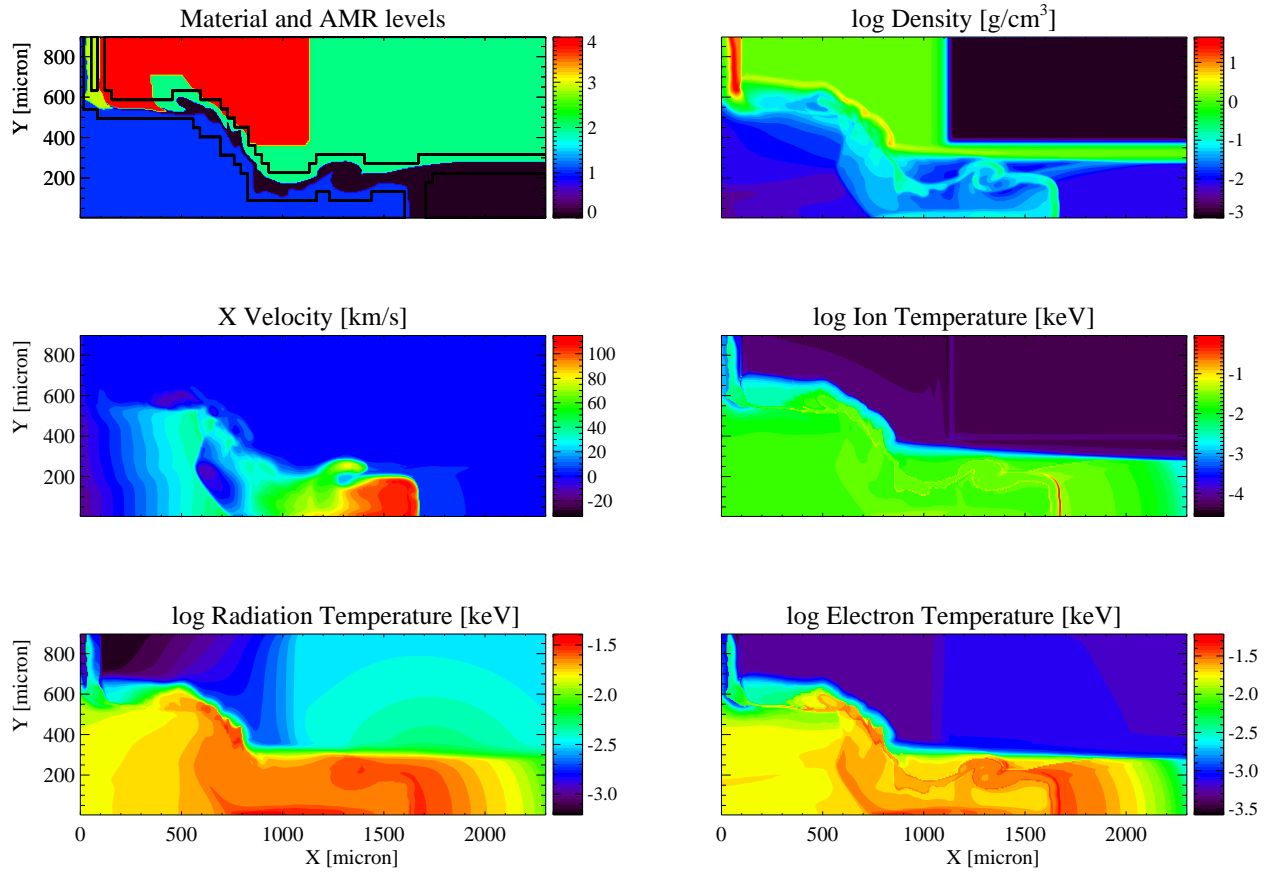
Fig. 17.— Simulated radiative shock structure at 13ns in a 3D elliptic nozzle consisting of the 5 materials indicated in Figure 16. The plots show in the xy-plane in color contour the variables indicated in the plot title. The primary shock is at $x \approx 1700$.
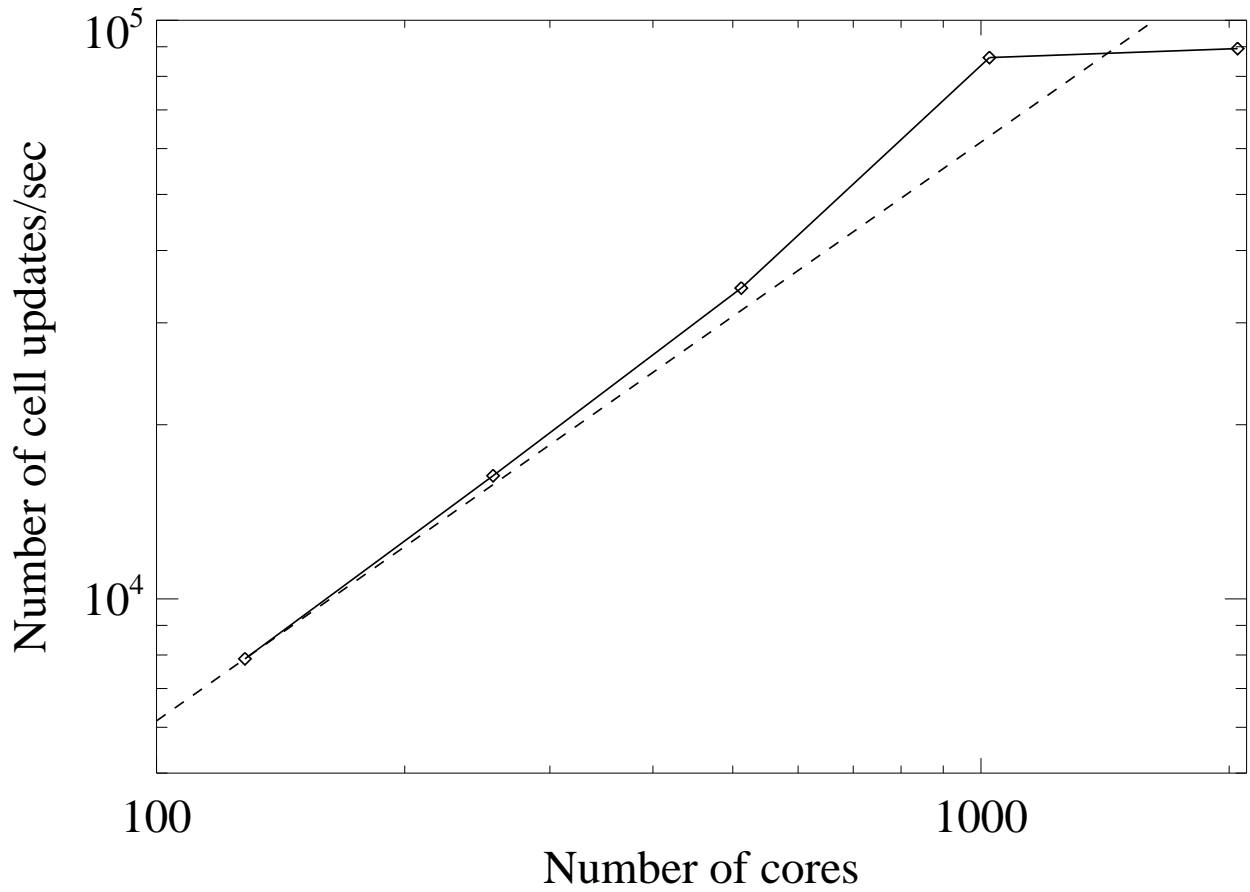
Fig. 18.— Strong scaling of the CRASH code, running a 3D CRASH application with 5 material level sets, electron and ion temperature, 30 radiation groups, and two levels of time dependent mesh refinement.
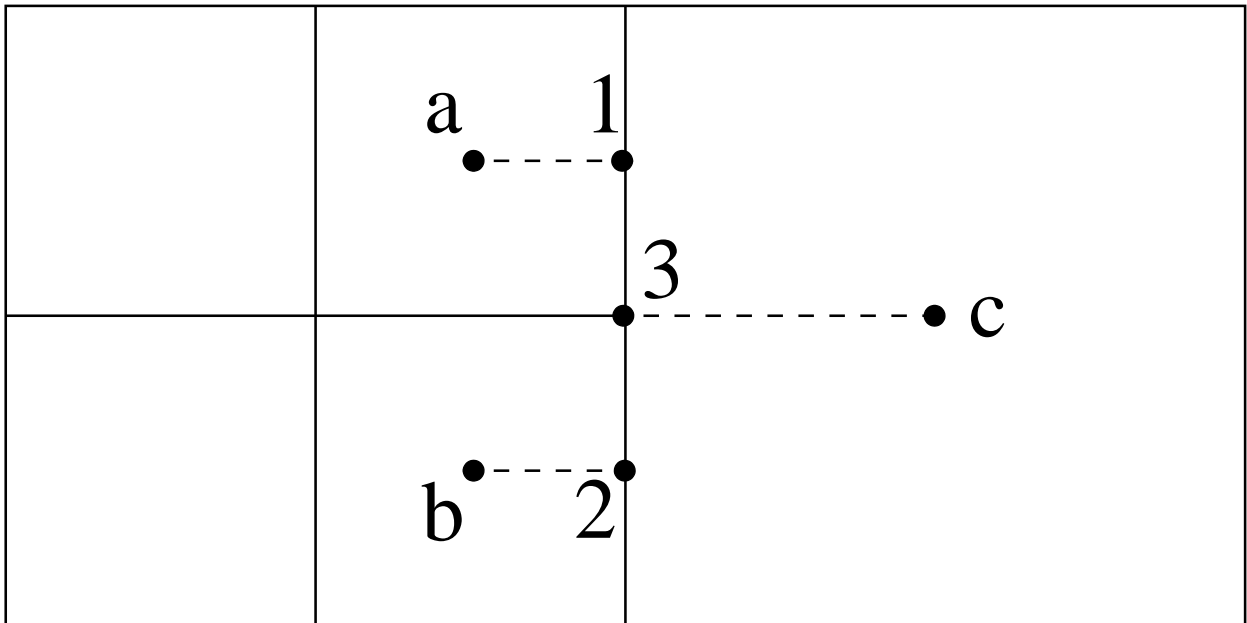
Fig. 19.— Cell and face centers at the adaptive interface in 2D.